

Structures of rhodopsin in complex with G-protein-coupled receptor kinase 1

<https://doi.org/10.1038/s41586-021-03721-x>

Received: 25 May 2020

Accepted: 11 June 2021

Published online: 14 July 2021

 Check for updates

Qiuyan Chen^{1,2}, Manolo Plasencia³, Zhuang Li¹, Somnath Mukherjee⁴, Dhabaleswar Patra^{1,2}, Chun-Liang Chen^{1,2}, Thomas Klose¹, Xin-Qiu Yao⁵, Anthony A. Kossiakoff^{4,6}, Leifu Chang¹, Philip C. Andrews^{3,7,8} & John J. G. Tesmer^{1,2}✉

G-protein-coupled receptor (GPCR) kinases (GRKs) selectively phosphorylate activated GPCRs, thereby priming them for desensitization¹. Although it is unclear how GRKs recognize these receptors^{2–4}, a conserved region at the GRK N terminus is essential for this process^{5–8}. Here we report a series of cryo-electron microscopy single-particle reconstructions of light-activated rhodopsin (Rho^*) bound to rhodopsin kinase (GRK1), wherein the N terminus of GRK1 forms a helix that docks into the open cytoplasmic cleft of Rho^* . The helix also packs against the GRK1 kinase domain and stabilizes it in an active configuration. The complex is further stabilized by electrostatic interactions between basic residues that are conserved in most GPCRs and acidic residues that are conserved in GRKs. We did not observe any density for the regulator of G-protein signalling homology domain of GRK1 or the C terminus of rhodopsin. Crosslinking with mass spectrometry analysis confirmed these results and revealed dynamic behaviour in receptor-bound GRK1 that would allow the phosphorylation of multiple sites in the receptor tail. We have identified GRK1 residues whose mutation augments kinase activity and crosslinking with Rho^* , as well as residues that are involved in activation by acidic phospholipids. From these data, we present a general model for how a small family of protein kinases can recognize and be activated by hundreds of different GPCRs.

The activation of GPCRs instigates intracellular signalling cascades that modulate a vast array of cellular processes⁹. Desensitization of these GPCRs is triggered by a small family of GRKs, which selectively phosphorylate either the third cytoplasmic loop or the C-terminal tail of activated receptors, thereby triggering the recruitment of arrestins and, typically, clathrin-mediated endocytosis¹. Because maladaptive overexpression of GRKs exacerbates conditions such as heart failure and cancer, GRKs have emerged as potentially important therapeutic targets^{10,11}.

The seven vertebrate GRKs (GRK1–GRK7) belong to the AGC kinase family and as such contain a protein kinase domain followed by a C-terminal extension (C-tail) (Fig. 1a). Located centrally within the C-tail is the active site tether (AST), a loop that contributes to the ATP binding site¹². The GRK kinase domain is inserted into a loop of a regulator of G-protein signalling homology (RH) domain—a bi-lobed helical bundle that bridges the small and large lobes of the kinase domain¹³. GRKs also feature a highly conserved, about 16-residue element at their extreme N termini. Truncation, antibody blockade, or mutation of this element can result in complete loss of activity towards receptor substrates^{5–8} (Extended Data Table 1). However, the mechanism by which GRKs recognize and are in turn activated by GPCRs has remained unresolved². Recent technical advances in cryo-electron microscopy (cryo-EM) have greatly facilitated the determination of structures of

GPCRs in complex with heterotrimeric G proteins and arrestins^{14–18}, which also selectively recognize activated GPCRs. Unfortunately, analogous GPCR–GRK structures are currently lacking, probably because such complexes are transient, dependent on anionic lipids, and of low- to mid-micromolar affinity¹⁹.

Rhodopsin and GRK1^{20,21} have co-evolved in the rod outer segments (ROSs) of photoreceptors to regulate scotopic vision since the emergence of vertebrates, and as such represent a highly optimized system for studying the GPCR–GRK interaction. Here we report four cryo-EM structures of the bovine Rho^* –GRK1 complex ranging from 7 to 4 Å resolution, crosslinking with mass spectroscopy (CLMS) analysis, and functional studies that reveal the molecular mechanism by which GRKs recognize activated GPCRs and provide a rare glimpse of a protein kinase being allosterically activated by its physiological substrate.

Isolation of the Rho^* –GRK1 complex

We first determined that the Michaelis constant (K_m) of GRK1 for Rho^* in lauryl maltose-neopentyl glycol (LMNG) micelles was sixfold lower than in native ROS membranes ($K_m > 5.8 \mu\text{M}$), and that the addition of 5% c8-phosphatidylinositol 4,5-bisphosphate (c8-PtdIns(4,5)P₂) further decreased the K_m twofold, to 0.33 μM. By contrast, the K_m for ATP remained constant (Fig. 1b, Extended Data Fig. 1a). We also documented

¹Department of Biological Sciences, Purdue University, West Lafayette, IN, USA. ²Department of Medicinal Chemistry and Molecular Pharmacology, Purdue University, West Lafayette, IN, USA.

³Department of Biological Chemistry, University of Michigan, Ann Arbor, MI, USA. ⁴Department of Biochemistry and Molecular Biology, University of Chicago, Chicago, IL, USA. ⁵Department of Chemistry, Georgia State University, Atlanta, GA, USA. ⁶Institute for Biophysical Dynamics, University of Chicago, Chicago, IL, USA. ⁷Department of Computational Medicine and Bioinformatics, University of Michigan, Ann Arbor, MI, USA. ⁸Department of Chemistry, University of Michigan, Ann Arbor, MI, USA. ✉e-mail: jtesmer@purdue.edu

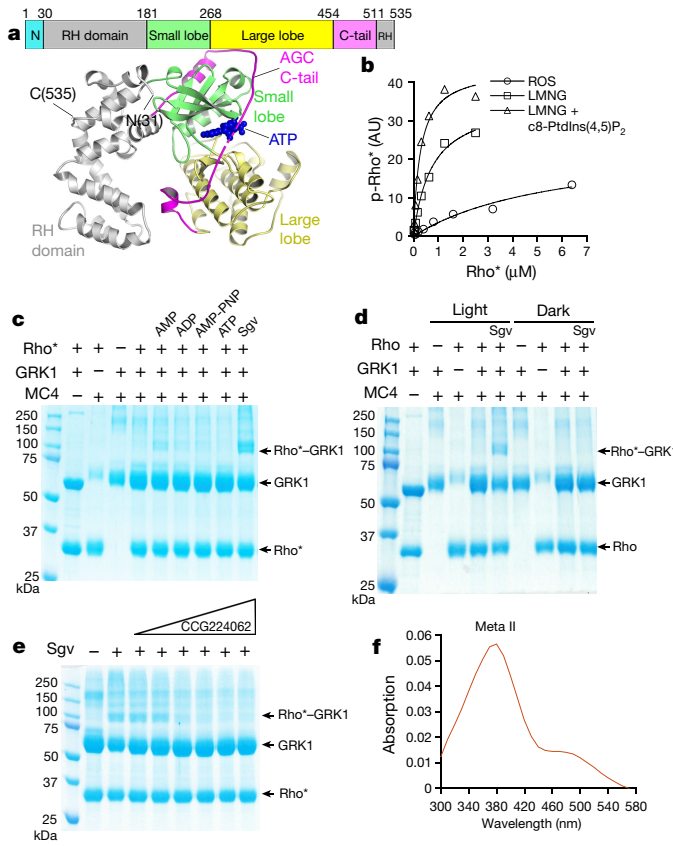


Fig. 1 | Trapping an activation-dependent complex between rhodopsin and GRK1. **a**, Primary structure of C-terminally truncated bovine GRK1 (residues 1–535) used in this study and its crystal structure in complex with ATP (Protein Data Bank (PDB) entry 3C4W⁴⁹), wherein the N terminus is disordered and the AST loop is partially ordered. **b**, Michaelis–Menten kinetics curves from a representative experiment out of three technical repeats with Rho* as substrate. Rhodopsin was solubilized with LMNG or LMNG + c8-PtdIns(4,5)P₂, and its kinetics were compared with those of rhodopsin in ROS. **c**, Crosslinking between Rho* and GRK1 in the presence of 1 mM AMP, ADP, AMP-PNP or ATP, or 0.8 mM Sgv (an adenosine analogue that helps to stabilize the active conformation of GRKs). **d**, Light dependence of the crosslinking reaction. **e**, Crosslinking in the presence of Sgv was progressively inhibited by increasing amounts (10–630 μM) of the GRK inhibitor CCG224062 ($I_{50} = 0.1 \text{ nM}$)²⁶, which stabilizes an inactive kinase domain conformation. For gel source data for **c–e**, see Supplementary Fig. 5a–c. **f**, The purified, crosslinked Rho*-GRK1 complex showed an absorption peak at 380 nm, consistent with rhodopsin being stabilized in its Meta II state.

a substantial increase in the activity of GRK1 against Rho* when incorporated into nanodiscs containing negatively charged lipids (Extended Data Fig. 1b, c), and then identified a cluster of basic residues in the GRK1 α helix, which bridges the small lobe and RH domain, that are involved in this activation (Supplementary Discussion, Extended Data Fig. 1c–e). Despite these improvements in apparent affinity and activity, we still could not purify an intact complex. Treating Rho* reconstituted in c8-PtdIns(4,5)P₂+LMNG micelles with the amine crosslinkers DC4²² and MC4²³ trapped a super-shifted species of about 100 kDa, consistent with the anticipated 1:1 Rho* (40 kDa)–GRK1 (61 kDa) complex²⁴ (Fig. 1c). Crosslinking was most efficient in the presence of sangivamycin (Sgv), an adenosine analogue with a 180 nM inhibition constant (K_i) against GRK1²⁵ that was previously used to trap GRK6 in what was proposed to be an active configuration⁶. Dark-adapted rhodopsin failed to crosslink (Fig. 1d) and an active site-directed small molecule inhibitor (CCG224062) that stabilizes GRKs in an inactive state²⁶ competed with crosslinking in a dose-dependent manner (Fig. 1e). The

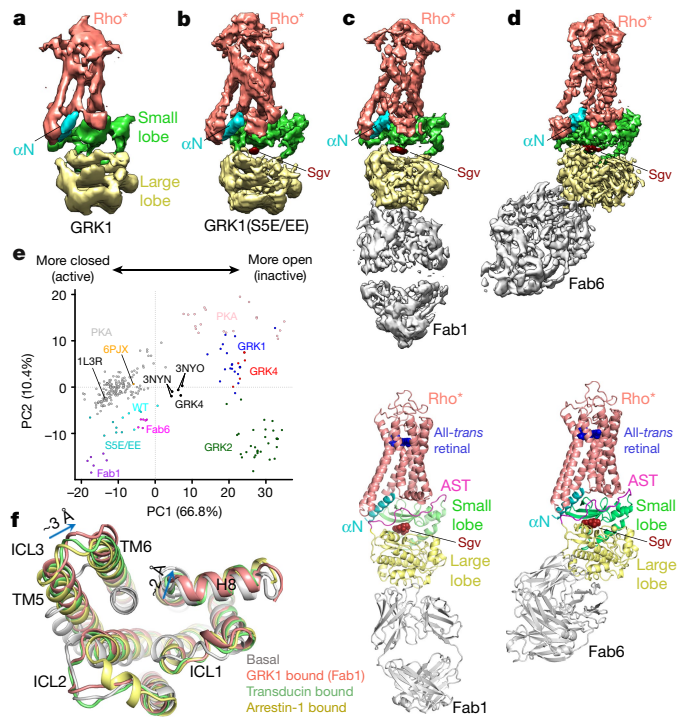


Fig. 2 | Cryo-EM single-particle reconstructions reveal the prominent role of the GRK1 α N helix and AST in forming the interface with Rho*.

a, **b**, Sharpened maps of the 7 Å Rho*-GRK1 (**a**) and 5.8 Å Rho*-GRK1(SSE/EE) (**b**) complexes. **c**, **d**, Sharpened maps (top) and models (bottom) of the Fab1-Rho*-GRK1(SSE/EE) complex (**c**) and the Fab6-Rho*-GRK1(SSE/EE) complex (**d**). **e**, PC analysis is consistent with a transition state-like conformation of the GRK1 kinase domain while in complex with Rho*. Each circle represents an individual experimental structure of the PKA kinase domain (grey, active; pink, inactive) or of the kinase domain from a member of one of the three GRK subfamilies: GRK1 (representing GRK1 and 7; various colours for active states, dark blue, inactive), GRK2 (GRK2 and 3; green, inactive), and GRK4 (GRK4, 5 and 6; black, active; red, inactive). Each structure was projected into the PC1–PC2 subspace, wherein PC1 and PC2 represent the directions with the largest conformational variance (67% and 10%, respectively). Molecular dynamics flexible fitting (MDFF) models 1–6 (Supplementary Table 1) of Rho*-GRK1 are coloured cyan, those of Rho*-GRK1(SSE/EE) dark cyan, Rho*-GRK1(SSE/EE)-Fab1 (Fab1) magenta, and Rho*-GRK1(SSE/EE)-Fab6 (Fab6) purple. PDB entry 1L3R is the transition state-like structure of PKA, 3NYN and 3NYO correspond to GRK6-Sgv/AMP complexes, and 6PJX is the Ca²⁺-CaM-GRK5 complex. PC1 and PC2 conformational changes are depicted in Supplementary Videos 3 and 4, respectively. **f**, Overlay of basal (PDB entry 1F88⁵⁰), GRK1-bound (7MTA), transducin-bound (6OYA¹⁴), and arrestin-1-bound (SWOP³¹) Rho*. Key differences between GRK1-bound and transducin or arrestin-1-bound Rho* structures are indicated with arrows.

absorption spectrum of the purified complex also confirmed the presence of metarhodopsin II (Meta II), the active form of rhodopsin (Fig. 1f). Thus, the isolated Rho*-GRK1 complex was dependent on the activated state of both GPCR and GRK. Crosslinking did not strongly depend on the phosphorylation status of Rho* or whether its C-terminal tail was truncated (Extended Data Fig. 1f, g).

Cryo-EM analysis

This purified complex (Supplementary Fig. 1) was vitrified for cryo-EM analysis, yielding a 7 Å severely anisotropic reconstruction (Fig. 2a, Extended Data Fig. 2, Extended Data Table 2). Interpretation of this map (Supplementary Discussion) suggested that affinity could be improved if GRK1 residues Ser5, Ser488, and Thr489, which are endogenous sites of autophosphorylation, were substituted with glutamic

acids (GRK1(SSE/EE)). This variant had a decreased K_m for Rho* and enhanced crosslinking yield, and improved the cryo-EM reconstruction to 5.8 Å (Fig. 2b, Extended Data Fig. 3, Extended Data Table 2). Two antigen-binding fragments (Fab1 and Fab6), selected against Sgv-bound GRK1, were then added to the Rho*-GRK1(SSE/EE) complex to increase particle size (by 50 kDa) and aid in particle alignment. These Fabs bind GRK1 with a low nanomolar affinity but have no effect on kinase activity towards Rho* (Extended Data Fig. 1h, i). Imaging of the Fab1 and Fab6 complexes yielded approximately 4 Å resolution cryo-EM reconstructions (Fig. 2c, d, Extended Data Figs. 4, 5, Extended Data Table 2, Supplementary Videos 1, 2). However, the data still showed a high degree of dynamic behaviour and a preferred orientation. When GRK1 in the Fab6 complex is superimposed with GRK1 in the other three structures, Rho* differs in orientation by about 5.5° relative to the small lobe (Extended Data Fig. 5e). It is unclear how Fab6 stabilizes this unique state. Density for Rho* is superior in the Fab1 complex, whereas density for intracellular loop 1 (ICL1) and helix 8 (H8) of Rho* are weak in the Fab6 complex. The overall density for GRK1 is, however, superior in the Fab6 complex.

Structure of the Rho*-GRK1 complex

In all reconstructions, the conformation of Rho* closely resembles that in its complex with transducin and arrestin-1 (root mean square deviations (r.m.s.d.) of 0.8 and 0.7 Å for 278 and 280 C α atoms, respectively). The Rho* model spans residues 1–324, ending after H8, and the density was consistent with the presence of all-trans retinal, although strong density was observed only for the ionone ring (Extended Data Fig. 6a), consistent with the fact that excess 11-cis retinal consistently increased crosslinking yield (Extended Data Fig. 6b). The GRK1 models contain residues 6–24 (comprising a single helix, α N), residues 182–508 (the kinase domain and C-tail), and Sgv, for which there is strong density in all reconstructions (Extended Data Fig. 6a). Density for residues 491–508 is weak, implying that this region is highly dynamic. Density was entirely lacking for the RH domain (Extended Data Fig. 6c), and its positional heterogeneity in the complex is also evident in negative-stain EM 2D class averages (Extended Data Fig. 6d).

In GRK1, α N packs against the AST and the small lobe, similar to its configuration in the GRK6-Sgv⁶ and Ca²⁺-CaM-GRK5²⁷ complexes (Extended Data Fig. 7a–d). GRK1-Asn12 is positioned to form hydrogen bonds with the side chain of GRK1-Arg191 on the small lobe—a position that is invariant in GRKs but not in other AGC kinases, and is essential for both GPCR and peptide phosphorylation^{5,28} (Extended Data Table 1)—and with GRK1-Asn480 in the AST (Fig. 3a, b). Consistent with this, the GRK1(N12A) mutation markedly reduced crosslinking (Fig. 3d). GRK1-Phe15 and GRK1-Phe22 are positioned to form hydrophobic contacts with hydrophobic residues in the small lobe and AST (Fig. 3c). Principal component (PC) analysis indicated that the GRK1 kinase domain is in a more active state (based on the dominant component PC1) in the Fab1 complex than in the other three reconstructions or in crystal structures of Sgv-bound GRK6⁶ and GRK5^{27,29,30} (Fig. 2e, Extended Data Fig. 7f–h). The differences in domain closure among the four reconstructions is likely to result from the high degree of dynamics in the complex, both in the hinge of the kinase domain and in the GRK interface with Rho*, consistent with the heterogeneous local resolution of the Fab1 and Fab6 complex maps (Extended Data Figs. 4d, 5d).

The Rho*-GRK1 interfaces in the Fab1 and Fab6 complexes bury 1,600 and 1,300 Å² of accessible surface area, respectively, comparable to and overlapping with that buried in transducin¹⁴ and arrestin-1³¹ complexes with Rho* (1,100 and 1,400 Å², respectively). Deviations in the backbone structure of GRK1-bound Rho* compared with transducin-bound or arrestin-1-bound Rho* (Fig. 2f, Supplementary Fig. 2) are well supported in the reconstructions. The cytoplasmic ends of Rho* transmembrane (TM) helices 5 and 6 in GRK1-bound Rho* adopt the expected outwards conformation relative to the TM core of dark state rhodopsin³² but TM6 is rotated away from its position in rhodopsin by about 20° in the GRK1

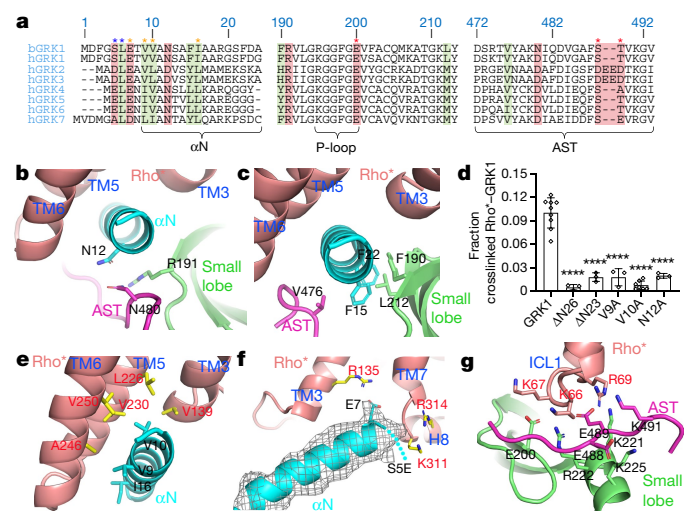


Fig. 3 | Interactions within GRK1 and Rho* involve highly conserved elements in each protein family. **a**, Sequence alignment of GRK N terminus, P-loop, and AST regions. The N-terminal Met of GRKs is expected to be cleaved, and in GRK2/3 the N-terminal residue is then acetylated⁵¹. Conserved hydrophobic residues involved in Rho* binding and kinase activation in GRK1 are highlighted in green, and conserved hydrophilic residues in red. Blue, orange, and red asterisks indicate GRK1 conserved residues that interact with Rho* H8, TM core, and ICL1, respectively. **b, c**, Interactions of α N with the GRK1 small lobe and AST in the Fab1 complex. **d**, Crosslinking yield of GRK1 α N variants compared to that of GRK1 using one-way ANOVA followed by a Dunnett's multiple comparison test (**** $P < 0.0001$). Error bars represent s.d. from three (V9A, N12A, Δ N₂₃, Δ N₂₆) or seven (V10A) technical replicates. For gel source data, see Supplementary Fig. 5d. **e–g**, Hydrophobic (**e**) and electrostatic (**f, g**) interactions of GRK1 α N with the cytoplasmic cleft of Rho* in the Fab1 complex. The approximate position of the GRK1(SSE) backbone is indicated by a dotted line. Electron density of GRK1 α N is shown as a wire cage contoured at 16σ. **g**, Interaction of GRK1(SSE/EE) with ICL1 of Rho*. Ser488 and Thr489 are autophosphorylation sites in GRK1 that are replaced by phosphomimetic glutamic acid residues in GRK1(SSE/EE).

complex, roughly 4° further than in the other two complexes, resulting in a shift of up to about 3 Å at the end of ICL3. This difference seems mandated by contacts formed by α N and residues 474 and 475 in the AST loop of GRK1 with TMs 5, 6, and ICL3. Rho* H8 is also shifted away from the receptor core by about 2 Å relative to the arrestin and transducin complexes. The end of TM1 and the first half of ICL1 shift with H8 (more so in Fab6 than Fab1). Key drivers for this difference may be the electrostatic interactions formed between the AST and ICL1, and the contacts between the N terminus of α N in GRK1 and H8. The end result is a wider, more open cytoplasmic cleft in Rho* when bound to GRK1.

Conservation of the Rho*-GRK1 interface

Modelling indicates that the mode of interaction exhibited by the Rho*-GRK1 complex will be compatible with other activated class A receptors such as the β 2 adrenergic receptor (β_2 AR) (Extended Data Fig. 7e, Supplementary Discussion). The most prominent feature in our maps is the α N of GRK1, which docks in the cytoplasmic cleft of Rho* in roughly the same way as the C-terminal helix of transducin¹⁴, although with opposite polarity and a trajectory that differs by about 25°, and in a manner that overlaps with the finger loop of arrestin-1 (Extended Data Fig. 7i–p). This is in contrast to several recently proposed receptor docking models for GRKs wherein α N has no direct role in the receptor interface² (Supplementary Discussion). Consistent with the importance of α N and previous studies, we showed that the crosslinking yield of the N-terminal truncations GRK1(Δ N23) and GRK1(Δ N26) was markedly

reduced (Fig. 3d, Extended Data Table 1). Residues Val9, Val10, and Ile16, which are important for agonist-dependent GPCR phosphorylation^{5,6,33,34}, pack against the hydrophobic inner surfaces of TM3, TM5 and TM6 (Fig. 3e). The V9A and V10A mutations also markedly reduced crosslinking yield (Fig. 3d). Conversely, mutation of Rho*-Leu226^{5,61} or -Val230^{5,65} (superscripts indicate Ballesteros–Weinstein nomenclature) to Ala in TM5 reduce Rho* phosphorylation by GRK1³⁵. Although density for GRK1(SSE) was not observed, its side chain would complement those of Rho*-Lys311^{8,48} and -Arg314^{8,51} (Fig. 3f), which are highly conserved in class A GPCRs (Supplementary Fig. 3). An acidic residue is conserved at the position of GRK1-Ser5 in most GRKs (Fig. 3a), and mutation of the homologous residue in GRK2 (D3A/K) substantially reduced its ability to phosphorylate the β_2 AR³³. GRK1-Glu7, which is highly conserved among GRKs but is less important for catalytic activity^{6,33,34} (Extended Data Table 1), is positioned so that it could form a salt bridge with Rho*-Arg135^{5,50}, one of the most highly conserved residues in class A receptors (Fig. 3f).

Rho* ICL1 forms more extensive interactions with GRK1 than with either transducin or arrestin-1 and contacts the AST loop near GRK1-Ser488 and Thr489 (Fig. 3g). The rapid autophosphorylation of these residues in vitro or in cells enhances Rho* phosphorylation^{36,37}. In our models, phospho-Ser488 could be coordinated by Rho*-Lys66 and GRK1-Lys225 and Lys491, and phospho-Thr489 by Rho*-Arg69 and GRK1-Lys221 and Arg222 (Fig. 3f). We validated this hypothesis via the GRK1(EE) and GRK1(SSE/EE) mutants, which exhibited lower K_m (SSE/EE) and enhanced crosslinking (EE and SSE/EE) (Extended Data Fig. 8a–g). Autophosphorylation of the homologous residues in GRK5 promotes its activity against activated receptors^{38,39} and GRK2/3 feature a cluster of phosphomimetic residues (DEED) that is predicted to be at its ICL1 contact site (Fig. 3a). Rho*-Lys67 in ICL1 is also positioned so that it could form a salt bridge with GRK1-Glu200 (Fig. 3f), an invariant P-loop residue in GRKs that is conserved as Arg or Lys in most other AGC kinases. The notable number of complementary interactions formed between basic residues in Rho* and acidic residues in GRK1 may explain the well-known sensitivity of GRK-mediated GPCR phosphorylation to ionic strength.

ICL1 is highly conserved in both sequence and structure among class A and B1 GPCRs (Supplementary Fig. 3), and even in cases where these receptors have structural differences, ICL1 retains basic residues that could favourably interact with GRKs and would still be able to bind GRK1 without steric collisions (data not shown). By contrast, class B2 (adhesion), C, and F GPCRs do not have analogous signatures in ICL1 (Supplementary Fig. 4). Class B2 (adhesion) and class F receptors do, however, have conserved basic residues in ICL1, and the recent structure of the adhesion receptor GPR97⁴⁰ suggests that its cytoplasmic cleft and ICL1 would be compatible with GRK binding despite large differences in other parts of the TM core. Class F receptors are difficult to assess for GRK compatibility given their distant structural homology. Notably, class C receptors do not seem to have ICL1 loops that would be compatible with GRK binding, even though metabotropic glutamate receptors are reported to be desensitized by GRKs^{41,42}. In some isoforms, such as metabotropic glutamate receptor 1 (mGlu1), this could occur by non-phosphorylation-dependent mechanisms such as the binding of the RH domain of GRK2 to activated G_{α_q} or directly to the receptor⁴². Meanwhile, mGlu2 receptors, but not mGlu3 receptors, are resistant to homologous desensitization by GRKs⁴³. Thus, there are complexities among mGluRs in their interactions with GRKs that cannot be explained by sequence comparison alone.

Rho*-ICL2 could not be confidently modelled in complex with GRK1 because of its continuity with the micelle boundary, but it is predicted to interact with the β_1 strand region of the small lobe of GRK1 and would collide with GRK1 α_0 if the helix were situated as in previous GRK1 crystal structures (Extended Data Fig. 8h). ICL3 contacts AST residues Arg474 and Thr475 (Extended Data Fig. 8i), but mutations at these positions in GRK1 did not measurably affect activity when

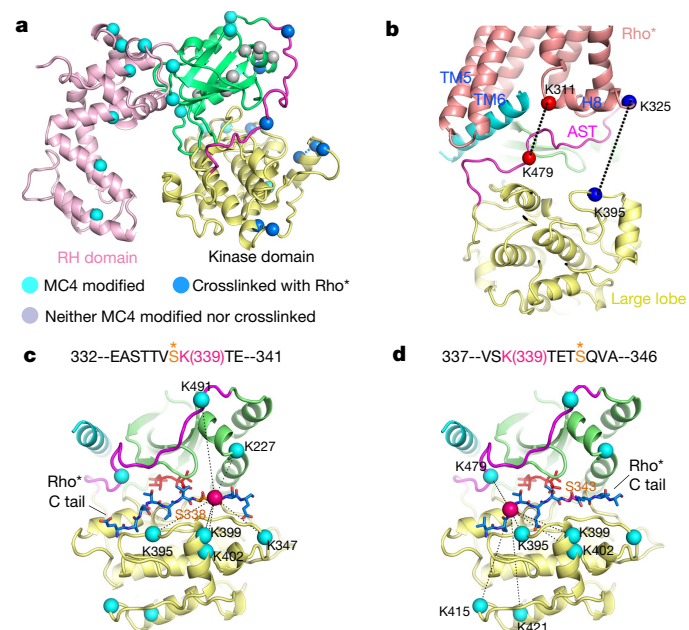


Fig. 4 | CLMS confirms the cryo-EM structure and reveals dynamics in the receptor C-terminal tail. **a**, Lysine residues of GRK1 that crosslink with Rho* are indicated by blue C α atoms, those that are dead-end modified are coloured cyan (suggesting solvent accessibility), and those that are unreactive are coloured grey (suggesting protection). **b**, Two prominent pairs of crosslinked lysines between Rho* and the kinase domain of GRK1 are highlighted with spheres connected by dashed lines. **c, d**, The C terminus of Rho* was modelled bound to the peptide-binding channel of GRK1 based on PDB entry 1O6L⁴⁵. Rho*-Lys339 C α is drawn as a red sphere, whereas the C α atoms of lysines on GRK1 that crosslink with it are cyan. ATP is coloured orange. **c**, Rho*-Ser338 in the phosphoacceptor site. **d**, Rho*-Ser343 in the phosphoacceptor site.

tested previously⁵ (Extended Data Table 1). By virtue of being located at the periphery of the interface, GPCRs with longer ICL3 loops would, however, not only have freedom to dock, but also have easy access to the active site of the bound GRK.

Validation by CLMS

The lysine residues on GRK1 that crosslinked with Rho* were all located on the kinase domain (Fig. 4a, Extended Data Fig. 9, Supplementary Tables 2, 3). Dead-end analysis, which identifies lysines modified by crosslinker and then quenched with either water or Tris buffer, was consistent with the RH domain not directly contributing to receptor binding because all of its lysines were detected in this analysis (Fig. 4a, cyan spheres; Supplementary Table 4). Lysines in the kinase domain that did not react are not accessible to solvent in the observed complex (Fig. 4a), consistent with the idea that a discrete GPCR–GRK complex forms in solution before the addition of crosslinker. Two major crosslinked regions between Rho* and GRK1 were identified (Fig. 4b–d, Supplementary Table 2). The first was between Rho*-Lys311^{8,48} and GRK1-Lys479 in the AST (Fig. 4b). The second was between two lysines in the Rho* C terminus and the phosphoacceptor binding cleft of the GRK1 kinase domain. Rho*-Lys325 crosslinks with GRK1-Lys395 in the large lobe (Fig. 4b), whereas Rho*-Lys339 also crosslinks with Lys325 and eight additional sites (Fig. 4c, d, Supplementary Table 2). Rho*-Lys339 is positioned between Ser338 and Ser343 (Fig. 4c, d), which are the primary phosphorylation sites in the C terminus of Rho*⁴⁴. When Ser338 is modelled at the phosphoacceptor site of the kinase domain⁴⁵, Lys339 can reach six out of the nine lysines in GRK1 identified by CLMS (Fig. 4c). Modelling instead Rho*-Ser343 at the active site places Rho*-Lys339 within range of the remainder of the GRK1 lysines identified (Fig. 4d).

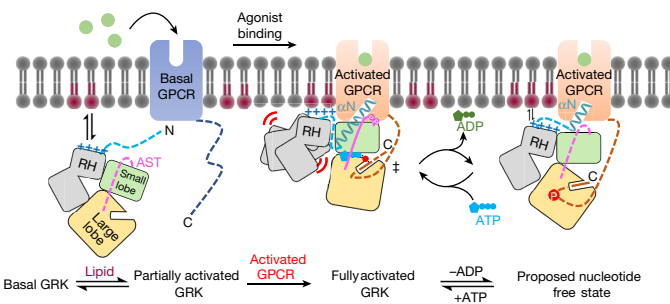


Fig. 5 | A generalized model for GRK activation by anionic lipids and activated GPCRs. In its basal state, the GRK kinase domain is in an open conformation with its small and large lobes engaged with both lobes of the RH domain. The N terminus and portions of the AST in the GRK are disordered. A basic region adjacent to the receptor interface (α O helix region in GRK1) promotes membrane association. Upon receptor activation, the GRK N terminus forms a helix (α N) that docks into the cytoplasmic cleft of the activated GPCR. α N also packs against the small lobe and AST to allosterically trigger kinase domain closure, aligning ATP with the phosphoacceptor in the C tail of GPCR in a transition state-like complex. GRKs may need to dissociate from the receptor at least partially to efficiently exchange adenine nucleotides, and in this state α N and the large lobe could remain bound to the cytoplasmic cleft and the phosphorylated tail of the receptor, respectively, to facilitate additional rounds of phosphorylation. In GRK1, and perhaps in the closely related GRK4 subfamily of GRKs, receptor binding also induces conformation changes that displace the RH domain. This could serve to strengthen membrane interactions mediated by the RH domain and its associated loops, including the α O helix. GRK2 and GRK3 lack an analogous α O helix and there is evidence that their RH domains may not be as dynamic in receptor complexes. Pink and red circles indicate GRK autophosphorylation and Rho* phosphorylation sites, respectively.

Thus, there is a high degree of dynamics in the receptor C terminus, which is consistent with its absence in our reconstructions and with the ability of Rho*-bound GRK1 to phosphorylate multiple sites in the receptor C terminus.

Discussion

Our Rho*-GRK1 reconstructions demonstrate that the few specific interactions formed in the Rho*-GRK1 interface involve sites that are highly conserved in both GRKs and most class A and B1 GPCRs. Our data also indicate that GPCRs activate GRKs by coalescing the α N and AST regions into a bridge that spans the small and large lobes of the kinase domain and stabilizes it in a more closed, catalytically competent state, consistent with early predictions⁶. GRK1 interacts with multiple regions of Rho* that are known to exhibit conformational changes in other GPCRs upon receptor activation. Despite the modest resolution of our maps, it is clear that these regions are distinct in conformation from those in Rho* complexes with transducin and arrestin-1 (Fig. 2f). Thus, our data indicate that some arrestin-biased ligands might function by stabilizing conformations of the GPCR that are more complementary to GRKs than to G proteins. Comparison with the recent G-protein- and arrestin-bound structures of the M2 muscarinic^{15,17} and neurotensin receptors^{16,18} also suggests that the conformation of Rho* in our structure is unique. We note that among the Rho*-interacting residues in GRK1, only Leu6 is invariant among GRKs. Thus, via ligand-induced changes in conformation, individual GPCRs could also change their selectivity for individual GRKs, leading to installation of distinct phosphorylation ‘barcodes’^{46,47} and hence different physiological outcomes.

Finally, our work provides insights into the overall process by which GRK phosphorylation of activated GPCRs occurs. In our current model, the α N helix of GRK1 is intrinsically disordered until it binds to activated

GPCRs in a form of ‘molecular fly-casting’⁴⁸ (Fig. 5). The fact that robust crosslinking to Rho* was not observed in the presence of either ATP or ADP suggests that GPCRs are optimized to bind GRKs in a conformation that is optimized for phosphotransfer, but not for ATP or ADP binding. A fly-casting mechanism would, however, allow for a partially dissociated state of the GRK wherein exchange of ADP for ATP could readily occur and enable further rounds of phosphorylation. Future studies are needed to validate this model and to examine how GRK2 and GRK4 subfamily members interact with receptors from the various GPCR classes, especially those lacking the interaction signatures defined by the Rho*-GRK1 complex.

Online content

Any methods, additional references, Nature Research reporting summaries, source data, extended data, supplementary information, acknowledgements, peer review information; details of author contributions and competing interests; and statements of data and code availability are available at <https://doi.org/10.1038/s41586-021-03721-x>.

- Gurevich, E. V., Tesmer, J. J., Mushegian, A. & Gurevich, V. V. G protein-coupled receptor kinases: more than just kinases and not only for GPCRs. *Pharmacol. Ther.* **133**, 40–69 (2012).
- Cato, M. C. et al. The open question of how GPCRs interact with GPCR kinases (GRKs). *Biomolecules* **11**, 447 (2021).
- Komolov, K. E. et al. Structural and functional analysis of a β_2 -adrenergic receptor complex with GRK5. *Cell* **169**, 407–421.e16 (2017).
- He, Y. et al. Molecular assembly of rhodopsin with G protein-coupled receptor kinases. *Cell Res.* **27**, 728–747 (2017).
- Beaurain, A. et al. Mapping the putative G protein-coupled receptor (GPCR) docking site on GPCR kinase 2: insights from intact cell phosphorylation and recruitment assays. *J. Biol. Chem.* **289**, 25262–25275 (2014).
- Boguth, C. A., Singh, P., Huang, C. C. & Tesmer, J. J. Molecular basis for activation of G protein-coupled receptor kinases. *EMBO J.* **29**, 3249–3259 (2010).
- Noble, B., Kallal, L. A., Pausch, M. H. & Benovic, J. L. Development of a yeast bioassay to characterize G protein-coupled receptor kinases. Identification of an NH₂-terminal region essential for receptor phosphorylation. *J. Biol. Chem.* **278**, 47466–47476 (2003).
- Palczewski, K., Buczko, J., Lebioda, L., Crabb, J. W. & Polans, A. S. Identification of the N-terminal region in rhodopsin kinase involved in its interaction with rhodopsin. *J. Biol. Chem.* **268**, 6004–6013 (1993).
- Lefkowitz, R. J. Seven transmembrane receptors: something old, something new. *Acta Physiol. (Oxf.)* **190**, 9–19 (2007).
- Brinks, H. & Koch, W. J. Targeting G protein-coupled receptor kinases (GRKs) in heart failure. *Drug Discov. Today Dis. Mech.* **7**, e129–e134 (2010).
- Nogués, L. et al. G protein-coupled receptor kinases (GRKs) in tumorigenesis and cancer progression: GPCR regulators and signaling hubs. *Semin. Cancer Biol.* **48**, 78–90 (2018).
- Kannan, N., Haste, N., Taylor, S. S. & Neuwald, A. F. The hallmark of AGC kinase functional divergence is its C-terminal tail, a cis-acting regulatory module. *Proc. Natl. Acad. Sci. USA* **104**, 1272–1277 (2007).
- Lodowski, D. T., Pitcher, J. A., Capel, W. D., Lefkowitz, R. J. & Tesmer, J. J. Keeping G proteins at bay: a complex between G protein-coupled receptor kinase 2 and G β y. *Science* **300**, 1256–1262 (2003).
- Gao, Y. et al. Structures of the rhodopsin-transducin complex: insights into G-protein activation. *Mol. Cell* **75**, 781–790.e3 (2019).
- Maeda, S., Qu, Q., Robertson, M. J., Skiniotis, G. & Kobilka, B. K. Structures of the M1 and M2 muscarinic acetylcholine receptor/G-protein complexes. *Science* **364**, 552–557 (2019).
- Huang, W. et al. Structure of the neurotensin receptor 1 in complex with β -arrestin 1. *Nature* **579**, 303–308 (2020).
- Staus, D. P. et al. Structure of the M2 muscarinic receptor- β -arrestin complex in a lipid nanodisc. *Nature* **579**, 297–302 (2020).
- Kato, H. E. et al. Conformational transitions of a neurotensin receptor 1-G α i complex. *Nature* **572**, 80–85 (2019).
- Pulvermüller, A., Palczewski, K. & Hofmann, K. P. Interaction between photoactivated rhodopsin and its kinase: stability and kinetics of complex formation. *Biochemistry* **32**, 14082–14088 (1993).
- Kühn, H. & Dreyer, W. J. Light dependent phosphorylation of rhodopsin by ATP. *FEBS Lett.* **20**, 1–6 (1972).
- Kühn, H., Cook, J. H. & Dreyer, W. J. Phosphorylation of rhodopsin in bovine photoreceptor membranes. A dark reaction after illumination. *Biochemistry* **12**, 2495–2502 (1973).
- Clifford-Nunn, B., Showalter, H. D. & Andrews, P. C. Quaternary diamines as mass spectrometry cleavable crosslinkers for protein interactions. *J. Am. Soc. Mass Spectrom.* **23**, 201–212 (2012).
- Hagen, S. E. et al. Synthesis of CID-cleavable protein crosslinking agents containing quaternary amines for structural mass spectrometry. *Org. Biomol. Chem.* **16**, 8245–8248 (2018).
- Baybutt, T. H. et al. Monomeric rhodopsin is sufficient for normal rhodopsin kinase (GRK1) phosphorylation and arrestin-1 binding. *J. Biol. Chem.* **286**, 1420–1428 (2011).
- Palczewski, K., Kahn, N. & Hargrave, P. A. Nucleoside inhibitors of rhodopsin kinase. *Biochemistry* **29**, 6276–6282 (1990).

26. Waldschmidt, H. V. et al. Structure-based design, synthesis, and biological evaluation of highly selective and potent G protein-coupled receptor kinase 2 inhibitors. *J. Med. Chem.* **59**, 3793–3807 (2016).
27. Komolov, K. E. et al. Structure of a GRK5–calmodulin complex reveals molecular mechanism of GRK activation and substrate targeting. *Mol. Cell* **81**, 323–339.e11 (2021).
28. Huang, C. C., Yoshino-Koh, K. & Tesmer, J. J. G. A surface of the kinase domain critical for the allosteric activation of G protein-coupled receptor kinases. *J. Biol. Chem.* **284**, 17206–17215 (2009).
29. Madhusudan, A., Akamine, P., Xuong, N. H. & Taylor, S. S. Crystal structure of a transition state mimic of the catalytic subunit of cAMP-dependent protein kinase. *Nat. Struct. Biol.* **9**, 273–277 (2002).
30. Yao, X. Q. et al. Navigating the conformational landscape of G protein-coupled receptor kinases during allosteric activation. *J. Biol. Chem.* **292**, 16032–16043 (2017).
31. Zhou, X. E. et al. Identification of phosphorylation codes for arrestin recruitment by G protein-coupled receptors. *Cell* **170**, 457–469.e13 (2017).
32. Farrens, D. L., Altenbach, C., Yang, K., Hubbell, W. L. & Khorana, H. G. Requirement of rigid-body motion of transmembrane helices for light activation of rhodopsin. *Science* **274**, 768–770 (1996).
33. Pao, C. S., Barker, B. L. & Benovic, J. L. Role of the amino terminus of G protein-coupled receptor kinase 2 in receptor phosphorylation. *Biochemistry* **48**, 7325–7333 (2009).
34. Huang, C. C., Orban, T., Jastrzebska, B., Palczewski, K. & Tesmer, J. J. Activation of G protein-coupled receptor kinase 1 involves interactions between its N-terminal region and its kinase domain. *Biochemistry* **50**, 1940–1949 (2011).
35. Jones Brunette, A. M., Sinha, A., David, L. & Farrens, D. L. Evidence that the rhodopsin kinase (GRK1) N-terminus and the transducin Ga C-terminus interact with the same “hydrophobic patch” on rhodopsin TM5. *Biochemistry* **55**, 3123–3135 (2016).
36. Kelleher, D. J. & Johnson, G. L. Characterization of rhodopsin kinase purified from bovine rod outer segments. *J. Biol. Chem.* **265**, 2632–2639 (1990).
37. Buczyłko, J., Gutmann, C. & Palczewski, K. Regulation of rhodopsin kinase by autophosphorylation. *Proc. Natl Acad. Sci. USA* **88**, 2568–2572 (1991).
38. Kunapuli, P., Gurevich, V. V. & Benovic, J. L. Phospholipid-stimulated autophosphorylation activates the G protein-coupled receptor kinase GRK5. *J. Biol. Chem.* **269**, 10209–10212 (1994).
39. Premont, R. T., Koch, W. J., Inglese, J. & Lefkowitz, R. J. Identification, purification, and characterization of GRK5, a member of the family of G protein-coupled receptor kinases. *J. Biol. Chem.* **269**, 6832–6841 (1994).
40. Ping, Y. Q. et al. Structures of the glucocorticoid-bound adhesion receptor GPR97-G_α complex. *Nature* **589**, 620–626 (2021).
41. Dhami, G. K. & Ferguson, S. S. Regulation of metabotropic glutamate receptor signaling, desensitization and endocytosis. *Pharmacol. Ther.* **111**, 260–271 (2006).
42. Dhami, G. K. et al. G Protein-coupled receptor kinase 2 regulator of G protein signaling homology domain binds to both metabotropic glutamate receptor 1a and Galphaq to attenuate signaling. *J. Biol. Chem.* **279**, 16614–16620 (2004).
43. Iacovelli, L. et al. Regulation of group II metabotropic glutamate receptors by G protein-coupled receptor kinases: mGlu2 receptors are resistant to homologous desensitization. *Mol. Pharmacol.* **75**, 991–1003 (2009).
44. Ohguro, H., Palczewski, K., Ericsson, L. H., Walsh, K. A. & Johnson, R. S. Sequential phosphorylation of rhodopsin at multiple sites. *Biochemistry* **32**, 5718–5724 (1993).
45. Yang, J. et al. Crystal structure of an activated Akt/protein kinase B ternary complex with GSK3-peptide and AMP-PNP. *Nat. Struct. Biol.* **9**, 940–944 (2002).
46. Reiter, E., Ahn, S., Shukla, A. K. & Lefkowitz, R. J. Molecular mechanism of β-arrestin-biased agonism at seven-transmembrane receptors. *Annu. Rev. Pharmacol. Toxicol.* **52**, 179–197 (2012).
47. Nobles, K. N. et al. Distinct phosphorylation sites on the β(2)-adrenergic receptor establish a barcode that encodes differential functions of β-arrestin. *Sci. Signal.* **4**, ra51 (2011).
48. Shoemaker, B. A., Portman, J. J. & Wolynes, P. G. Speeding molecular recognition by using the folding funnel: the fly-casting mechanism. *Proc. Natl Acad. Sci. USA* **97**, 8868–8873 (2000).
49. Singh, P., Wang, B., Maeda, T., Palczewski, K. & Tesmer, J. J. Structures of rhodopsin kinase in different ligand states reveal key elements involved in G protein-coupled receptor kinase activation. *J. Biol. Chem.* **283**, 14053–14062 (2008).
50. Palczewski, K. et al. Crystal structure of rhodopsin: a G protein-coupled receptor. *Science* **289**, 739–745 (2000).
51. Pitcher, J. A. et al. Feedback inhibition of G protein-coupled receptor kinase 2 (GRK2) activity by extracellular signal-regulated kinases. *J. Biol. Chem.* **274**, 34531–34534 (1999).

Publisher's note Springer Nature remains neutral with regard to jurisdictional claims in published maps and institutional affiliations.

© The Author(s), under exclusive licence to Springer Nature Limited 2021

Methods

No statistical methods were used to predetermine sample size. The experiments were not randomized and investigators were not blinded to allocation during experiments and outcome assessment.

Expression and purification of GRK1

Full-length bovine GRK1 (residues 1–561) has a farnesylation site at its C terminus that limits its expression in insect cells. We therefore used truncated GRK1 (residues 1–535, hereafter referred to simply as GRK1). This variant exhibits slightly decreased kinase activity towards the receptor relative to the wild type³⁵. A His₆-tag was added to the C terminus of GRK1 for metal affinity purification⁴⁹. The mutagenesis and cloning of GRK1 has previously been described³⁴. We used the Bac-to-Bac baculovirus expression system (Invitrogen) to express GRK1 in either *Spodoptera frugiperda* or *Trichoplusia ni* insect cells (used without authentication or testing for mycoplasma). For purification, freshly prepared or thawed cell pellets were resuspended in cold lysis buffer (buffer A) containing 20 mM HEPES (pH 8.0), 400 mM NaCl, 2 mM DTT, 0.1 mM PMSF and leupeptin, lima bean trypsin protease inhibitor. The cells were resuspended using a dounce homogenizer and then lysed using an Avestin C3 emulsifier. The lysed cells were centrifuged in a Beckman Ti-45 rotor at 45,000 rpm for 45 min. The supernatant was combined and filtered through a glass filter and loaded onto a 2-ml home-packed Ni²⁺-NTA column pre-equilibrated with buffer A. The column was then washed with 50 ml buffer A, followed by 50 ml buffer A plus 20 mM imidazole. The bound protein was eluted in approximately 2-ml fractions with buffer A plus 200 mM imidazole. The purity of GRK1₅₃₅-His₆ after this step was about 95% as revealed by Coomassie blue staining of samples assessed via SDS-PAGE. The fractions were pooled and concentrated with a 50-kDa cutoff 50-ml centrifugal concentrator (Amicon Ultra) to about 1–2 ml. Then, 0.5 ml of the concentrated sample was injected onto a Superdex 200 Increase column (GE healthcare) equilibrated with buffer containing 20 mM HEPES (pH 8.0), 150 mM NaCl, and 0.5 mM TCEP. The peak fractions were pooled and concentrated to about 10 mg/ml, flash frozen in liquid nitrogen and stored at –80 °C for future use. We produced GRK1 variants (V9A, V10A, N12A, SSE, EE(S488E/T489E), DD(S488D/T489D) and SSE/EE) using the same procedure. For GRK1(ΔN₂₆), GRK1(ΔN₂₃) and GRK(5A) (R31A/R33A/K34A/R38A/K40A), which showed decreased expression levels, an extra ion-exchange step using a 1-ml HiTrap Q column (GE Healthcare) was performed after metal affinity purification. For this step, protein eluted from an Ni²⁺-NTA column was diluted tenfold with 20 mM HEPES, 2 mM DTT before loading onto the Q column. GRK1 variants were eluted at about 100 mM NaCl.

Preparation of ROS from bovine retinas

All procedures were conducted in a dark room under red light as previously described⁵⁸. In brief, about 100 retinas were resuspended with about 100 ml of 45% (w/v) sucrose in buffer B containing 70 mM phosphate buffer (pH 7.0), 1 mM MgCl₂ and 0.1 mM EDTA and were shaken vigorously by hand for about 3 min, and then the sample was centrifuged at 5,000 rpm for 5 min. The supernatant was filtered through four layers of cheesecloth, diluted 1:1 with buffer B and centrifuged at 13,000 rpm for 10 min. The pellet was then resuspended with 25.5% sucrose and overlaid on top of two sucrose layers containing 14 ml of 32.25% sucrose with 13 ml of 27.125% sucrose. The sucrose gradient was centrifuged in a swinging bucket rotor (SW-27) at 18,000 rpm for 90 min. ROS settled between the two layers and were collected using a syringe. The collected ROS were washed twice with buffer B to remove sucrose, incubated with 5 M urea for 10 min, and then washed three times with 20 mM HEPES (pH 8.0), 2 mM MgCl₂. The ROS were aliquoted and stored at –80 °C for future use.

Preparation of hyper-phosphorylated rhodopsin

We incubated 2 μM of ROS with 100 nM GRK1 under ambient light at room temperature for one hour in a buffer containing 50 mM HEPES

(pH 8.0), 500 μM ATP, and 10 mM MgCl₂. An γ-P³²-ATP standard curve estimated 6–8 phosphates incorporated per rhodopsin, indicating full saturation given that there are only 7 possible sites in the cytoplasmic tail of the receptor. After phosphorylation, the membrane was washed twice with 20 mM HEPES (pH 8.0) and 100 mM NaCl and then incubated with tenfold molar excess of 11-cis retinal in the dark at room temperature for 1 h for the purpose of regeneration.

Preparation of Asp-N treated rhodopsin

We incubated 0.5 mg of ROS with 0.4 μg of Asp-N protease (Roche) overnight at room temperature in the dark. Asp-N treated ROS was washed twice with buffer containing 20 mM HEPES (pH 8.0) and 100 mM NaCl before detergent reconstitution.

Rhodopsin reconstitution in detergent micelles

We added 500 μl of 5 mM LMNG to 100 μg of c8-PtdIns(4,5)P₂ powder to make 5% (molar ratio) c8-PtdIns(4,5)P₂ + LMNG micelles. Rhodopsin reconstitution was performed under dim light in a dark room. We used 400 μl of the c8-PtdIns(4,5)P₂ + LMNG solution to dissolve 0.5 mg of rhodopsin in ROS membrane. After incubation on ice for 30 min, the solution was centrifuged at 13,000 rpm for 10 min to pellet insoluble material. The supernatant, containing rhodopsin solubilized with c8-PtdIns(4,5)P₂ + LMNG, was isolated and its concentration assessed using a Bradford assay. The same procedure was followed to reconstitute rhodopsin with LMNG alone.

Rhodopsin reconstitution in nanodiscs

All lipids used for nanodiscs were purchased from Avanti dissolved in chloroform. We mixed 40% 1-palmitoyl-2-oleoyl-sn-glycero-3-phospho-L-serine (POPS) or 1-palmitoyl-2-oleoyl-sn-glycero-3-phospho-(1'-rac-glycerol) (POPG) with 60% 1-palmitoyl-2-oleoyl-sn-glycero-3-phosphocholine (POPC) and the chloroform was dried under a gentle stream of N₂. The glass vials containing the mixed lipids were kept in a desiccator overnight to remove any residual chloroform. CHAPS detergent was added to dissolve the lipids until it became a clear solution. Lipids, MSP1D1 and Rho were mixed at a ratio of 360:6:1 in the dark for 30 min. Biobeads were added to the mix and incubated overnight. The reconstituted Rho was loaded onto a Superdex 200 increase column in buffer containing 20 mM HEPES (pH 8.0) and 100 mM NaCl under lighted conditions. The peak fractions containing either empty nanodiscs or nanodiscs with rhodopsin were pooled and concentrated using a 100-kDa cutoff 50-ml centrifugal concentrator (Amicon Ultra). The amount of rhodopsin reconstituted in nanodiscs was determined using Coomassie staining with known amount of rhodopsin as standard.

Crosslinker screening

To screen for conditions that covalently capture a Rho*-GRK1 complex, 10 μM GRK1 and 10 μM rhodopsin reconstituted with c8-PtdIns(4,5)P₂ + LMNG was mixed in the absence or presence of various adenosine analogues (1 mM AMP, 1 mM ADP, 1 mM AMP-PNP, 1 mM ATP, or 0.8 mM Sgv) and incubated in the dark for 20 min on ice. Crosslinkers were dissolved with buffer containing 50 mM HEPES (pH 8.0) and 10 mM MgCl₂ immediately before use and added to the reaction. The samples were exposed to ambient light on ice for 30 min to activate rhodopsin and SDS sample buffer was used to quench the reaction. The crosslinking result was assessed using Coomassie blue staining of proteins separated by 10% SDS-PAGE. We screened seven crosslinkers: BS3, BS(PEG)₅, BM(PEG)₂, BM(PEG)₃ (ThermoFisher) and PC4, DC4²² and MC4²³ (provided by the Andrews laboratory, University of Michigan). Both DC4 and MC4 successfully crosslinked rhodopsin and GRK1 in the presence of Sgv.

Testing of conditions necessary for crosslinking

The same experiment used in the crosslinker screening was used to assess the effect of receptor activation and GRK ligands on crosslinking

Article

in the presence of 2 mg/ml MC4. To assess the light dependence of crosslinking, one reaction was kept in the dark throughout and was compared with a reaction pre-exposed to light for 30 min. To test the effect of an inhibitor that traps GRK1 in an inactive state, 10 μ M GRK1, 10 μ M rhodopsin and 0.4 mM Sgv were incubated along with increasing concentrations of CCG224062 (from 0.01 to 0.63 mM) for 20 min in the dark before light activation. All crosslinking experiments were repeated at least three times. For quantification, the density of crosslinked Rho*-GRK1 complex was normalized to the combined density of Rho* and GRK1 without crosslinker as an estimation of crosslinking efficiency and was used to compare between groups.

The purification of the crosslinked Rho*-GRK1 complex

Although c8-PtdIns(4,5)P₂ did not significantly enhance the crosslinking between Rho* and GRK1 (Supplementary Fig. 5e), it was kept in the reaction for complex purification. A crosslinking reaction with a total volume of 5.0 ml was set up as described above. We added 50 mM Tris (pH 8.0) to quench the reaction. The reaction mix was loaded onto a 1-ml HiTrap Q column (GE Healthcare) equilibrated with 20 mM HEPES (pH 8.0), 100 mM NaCl, 0.2 mM MgCl₂, 0.2 mM LMNG and 20 μ M Sgv. GRK1 and crosslinked Rho*-GRK1 complex were eluted over a gradient of 100–200 mM NaCl. Rhodopsin and self-crosslinked rhodopsin eluted at 500 mM NaCl. The fractions containing primarily crosslinked Rho*-GRK1 complex and some GRK1 were pooled together and concentrated with a 100-kDa cutoff 50-ml concentrator (Amicon Ultra) to about 400 μ l. The concentrated sample was loaded onto a Superdex 200 Increase column equilibrated with 20 mM HEPES (pH 8.0), 100 mM NaCl, 0.2 mM MgCl₂, 0.2 mM LMNG and 20 μ M Sgv. The crosslinked Rho*-GRK1 complex eluted at a volume consistent with a 150-kDa globular protein and was pooled for EM and CLMS analysis. The yellow colour of the final sample was consistent with the retention of all-trans retinal in the sample, and also showed an absorption peak at 380 nM, indicating that Rho* was in the Meta II state (Fig. 1f).

Michaelis–Menten kinetic analysis

In Fig. 1b and Extended Data Fig. 1a, K_m and V_{max} for Rho* were determined by varying Rho* concentrations from 0.05 to 6 μ M for ROS and from 0.02 to 2.5 μ M for rhodopsin reconstituted in LMNG or c8-PtdIns(4,5)P₂ + LMNG. The lower concentration range used for rhodopsin reconstituted with detergent was necessary because GRK1 kinase activity is inhibited by detergent at high concentrations. The reactions contain 50 nM GRK1, 20 μ M ATP (500 Ci/mol) and 50 mM HEPES (pH 8.0), 10 mM MgCl₂. K_m and V_{max} for ATP were determined by varying ATP concentrations from about 0.16 to 20 μ M (500 Ci/mol) in reactions containing 50 nM GRK1, 1 μ M rhodopsin, 50 mM HEPES (pH 8.0) and 10 mM MgCl₂. Rhodopsin was activated under an ambient light for 1 min before the reaction. The reaction proceeded for 2 min at room temperature and was quenched with SDS sample buffer. Rho* and GRK1 were separated by SDS-PAGE and the extent of phosphorylation was assessed using image analysis with the Quantity One program (BioRad) on phosphor screens. Plots of initial velocity versus concentration of the varied substrates were fit to the Michaelis–Menten equation using GraphPad prism. For Extended Data Fig. 1b, the same procedure was performed as described above except that the range of ROS was varied from 0.15 to 18 μ M when determining the K_m and V_{max} for Rho*. When comparing how nanodiscs affected GRK1 kinetics, lower amounts of Rho* were used. For Extended Data Fig. 8c–e, the same procedure was performed as described above except that the reaction contained 0.1 μ M rhodopsin instead of 1 μ M when determining the K_m and V_{max} for ATP.

Analysis of tubulin phosphorylation by GRK1 and mutants

Phosphorylation reactions contained 5 μ M tubulin (PurSolutions), 50 nM GRK1, 5 μ M ATP, 50 mM HEPES (pH 8.0) and 10 mM MgCl₂. The reaction was quenched at 2, 5, 10, 20 and 30 min with SDS sample buffer. Tubulin and GRK1 were separated by SDS-PAGE and the

extent of phosphorylation was assessed using image analysis with the Quantity One program (BioRad) on phosphor screens. This assay was repeated three times.

Preparation of biotinylated GRK1

An Avi-tag was added to the GRK1 C terminus after the His₆-tag. The same procedures used to produce GRK1 as described above were used to generate Avi-tagged GRK1. BirA500 kit (Avidity) was used to biotinylate Avi-tagged GRK1. In brief, 2 mg Avi-tagged GRK1 was incubated with 8 μ l biotin ligase, 80 μ l biomix A and 80 μ l biomix B supplied from the kit overnight on ice. The biotinylated GRK1 was loaded onto a Superdex 200 Increase column with buffer containing 20 mM HEPES (pH 8.0), 100 mM NaCl and 0.2 mM TCEP. The monomeric peak was collected and concentrated using a 50-kDa cutoff 50-ml concentrator (Amicon Ultra) to about 10 mg/ml. The biotinylation efficiency was estimated to be close to 100% by pull-down experiments using Streptavidin magnetic beads.

Phage display selections

Sgv-bound biotinylated GRK1 was used as target for phage display selection, performed at 4 °C according to published protocols³⁹ in a selection buffer supplemented with 10 μ M Sgv. In brief, in the first round, 100 nM of target was immobilized on 250 μ l of magnetic beads. Then, 100 μ l of a phage library E⁶⁰ containing 10¹²–10¹³ virions was added to the Streptavidin beads and incubated for 30 min. The resuspended beads containing bound virions were washed extensively and then used to infect freshly grown log-phase *Escherichia coli* XL1-Blue cells (Agilent). Phages were amplified overnight in 2 \times YT medium with 50 μ g/ml ampicillin and 10⁹ plaque-forming units (PFU) per ml of M13-KO7 helper phage. To increase the stringency of selection, three additional rounds of sorting were performed with the target concentration decreasing in each round (second round: 50 nM, third round: 10 nM and fourth round: 10 and 5 nM) using the amplified pool of virions of the preceding round as the input. Selection from the second to fourth rounds was done on a Kingfisher instrument using a solution capture method wherein the target was premixed with the amplified phage pool and then Streptavidin beads were added to the mixture. From the second round onwards, the bound phages were eluted using 0.1 M glycine (pH 2.7). This elution technique often risks the elution of non-specific and Streptavidin binders, which tend to overpopulate the amplified phage pool and thereby reduce the chance to obtain the desired specific clones. To eliminate them, the precipitated virions from the second round onwards were negatively selected against 100 μ l of Streptavidin beads before adding to the target. The pre-cleared phage pool was then used as an input for the selection.

Single-point phage ELISA

All enzyme-linked immunosorbent assay (ELISA) experiments were performed at 4 °C in 96-well plates coated with 50 μ l of 2 μ g/ml neutravidin in Na₂CO₃ buffer (pH 9.6) and subsequently blocked by 0.5% bovine serum albumin (BSA) in PBS. A single-point phage ELISA was used to rapidly screen the binding of the obtained Fab fragments in phage format. Colonies of *E. coli* XL1-Blue harbouring phagemids from the fourth round of selection were inoculated directly into 500 μ l of 2 \times YT broth supplemented with 100 μ g/ml ampicillin and M13-KO7 helper phage. The cultures were grown overnight at 37 °C in a 96-deep-well block plate. HBS with 0.05% (v/v) Tween-20 supplemented with 10 μ M Sgv was used in the ELISA. Culture supernatants containing Fab phage were diluted tenfold in HBST buffer in the presence of 10 μ M Sgv. After 15 min of incubation, the mixtures were transferred to ELISA plates that were incubated with 30 nM biotinylated GRK1 in experimental wells and with buffer in control wells for 15 min. The ELISA plates were incubated with the phage for another 15 min and then washed with ELISA buffer. The washed ELISA plates were incubated with a 1:1 mixture of mouse anti-M13 monoclonal antibody (cat: 27-9420-01, GE, 1:5,000 dilution in

ELISA buffer) and peroxidase-conjugated goat anti-mouse IgG (cat: 115-035-003, Jackson ImmunoResearch, 1:5,000 dilution in ELISA buffer) for 30 min. The plates were again washed, developed with TMB substrate and then quenched with 1.0 M HCl, and the absorbance at 450 nm was determined. The background binding of the phage was monitored by the absorbance from the control wells.

Sequencing, cloning, overexpression and purification of Fab fragments

From phage ELISA, clones (selected on the basis of a high ratio of ELISA signal of target binding to background) were sequenced at the DNA Sequencing Facility at the University of Chicago. Unique clones were sub-cloned in pRH2.2, an IPTG inducible vector for the expression of Fabs in *E. coli*. *Escherichia coli* C43 cells were transformed with sequence-verified clones of Fab fragments in pRH2.2. Fab fragments were grown in TB autoinduction medium with 100 µg/ml ampicillin overnight at 30 °C. Collected cells were kept frozen at -80 °C until use. Frozen pellets were re-suspended in PBS supplemented with 1 mM PMSF and 1 µg/ml DNaseI. The suspension was lysed by ultrasonication. The cell lysate was incubated at 65 °C for 30 min to eliminate any undesired proteolysed fragments of the Fab produced during over-expression. Heat-treated lysate was then cleared by centrifugation, filtered through 0.22-µm filter and loaded onto a HiTrap Protein L 5-ml column pre-equilibrated with lysis buffer (20 mM HEPES buffer, pH 7.5, 500 mM NaCl). The column was washed with 10 column volumes of lysis buffer followed by elution of Fab fragments with elution buffer (0.1 M acetic acid). Fractions containing protein were directly loaded onto a Resource S1-ml column pre-equilibrated with buffer A (50 mM sodium acetate, pH 5.0) followed by washing with 10 column volumes of buffer A. Fab fragments were eluted with a linear gradient 0–50% of buffer B (50 mM sodium acetate, pH 5.0, 2.0 M NaCl). Affinity and ion-exchange chromatography were performed using an automated program on an ÄKTA explorer system. Purified Fab fragments were dialysed overnight against 20 mM HEPES (pH 7.4) and 150 mM NaCl. The quality of purified Fab fragments was analysed by SDS-PAGE.

Multipoint protein ELISA for EC₅₀ determination

Multipoint ELISA was performed at 4 °C to estimate the affinity of the Fabs to GRK1. HBS with 0.05% (v/v) Tween-20 supplemented with 10 µM Sgv was used as the ELISA buffer. We incubated 30 nM of Sgv-bound biotinylated GRK1 immobilized on a neutravidin-coated ELISA plate with threefold serial dilutions of the purified Fabs starting from 4 µM for 20 min. The plates were washed, and the bound GRK1–Fab complexes were incubated with a secondary HRP-conjugated Pierce recombinant protein L (cat: 32420, Thermo Fisher, 1:5,000 dilution in ELISA buffer) for 30 min. The plates were again washed, developed with TMB substrate and quenched with 1.0 M HCl, and absorbance at 450 nm was measured. To determine the affinities, the data were fitted in a dose-response sigmoidal function in GraphPad PRISM and EC₅₀ values were calculated.

Cryo-EM sample preparation and image acquisition

Purified Rho*-GRK1(SSE/EE) complex at about 0.3 mg/ml was incubated with 1.2 molar excess of Fab1 or Fab6 for 20 min before freezing. Grids of Rho*-GRK1, Rho*-GRK1(SSE/EE), Rho*-GRK1(SSE/EE)–Fab1, or Rho*-GRK1(SSE/EE)–Fab6 were prepared using the same procedure. Samples at about 0.3 mg/ml were applied onto glow-discharged 300 mesh grids (Quantifoil R1.2/1.3) and plunge-frozen into liquid ethane using a FEI Vitrobot Mark IV (Thermo Fisher Scientific). Data were collected on a Titan Krios electron microscope operated at 300 kV using Leginon⁶¹ with a nominal magnification of 81,000× (resulting in a calibrated physical pixel size of 1.08 Å/pixel) and a defocus range of 1.2–2.5 µm. The images were recorded on a K3 summit electron direct detector (Gatan) in super-resolution mode at the end of a GIF-Quantum energy filter (Gatan) operated with a slit width of 20 eV. A dose rate of 20 e⁻/pix/s and an exposure time of 3.12 s were used, generating 40 movie frames with a total dose of about 54 electrons per Å².

EM data processing

For the Rho*-GRK1 complex reconstruction, movie frames were imported to RELION-3⁶² and aligned using MotionCor2⁶³ with binning factor of 2. Contrast transfer function (CTF) parameters were estimated using Gctf⁶⁴. Laplacian-of-Gaussian picking was used to pick about 2.68 million particles, which were extracted from the dose-weighted micrographs. The dataset was split into batches for multiple rounds of 2D classifications to exclude bad particles that fell into 2D averages with poor features. After this cleaning step, 705,966 particles remained. Particles from different views were used to generate an initial model in cryoSPARC⁶⁵. Further 3D classification with three classes was performed to select the class with resolvable secondary structure features. The selected 183,717 particles were used for final 3D refinement in RELION-3⁶², converging at 7 Å global resolution, as determined by the Fourier shell correlation (FSC) criterion in RELION-3 PostProcess⁶². The data processing workflow is shown in Extended Data Fig. 2. For the Rho*-GRK1(SSE/EE), Rho*-GRK1(SSE/EE)–Fab1 and Rho*-GRK1(SSE/EE)–Fab6 complexes, the movie frames were first motion-corrected using MotionCor2⁶³ with binning factor of 2 and then imported into cryoSPARC⁶⁵. CTF parameters were estimated using patch CTF. Blob Picker was used to pick from 100 micrographs and the selected particles were processed via 2D classification. The good 2D classes were selected and used as templates for Template Picker to pick particles from all micrographs. The picked particles were extracted from the dose-weighted micrographs. Multiple rounds of 2D classifications were performed to exclude bad particles that fell into 2D averages with poor features. The remaining particles from different views were used to generate an initial model in cryoSPARC⁶⁵. For Rho*-GRK1(SSE/EE), particles were imported into RELION-3⁶² and further 3D classification with six classes was performed to select the class with resolvable secondary structure features. The selected 132,721 particles were used for final 3D refinement in RELION-3⁶², converging at 5.8 Å global resolution, as determined by the FSC criterion in RELION-3 PostProcess⁶². The data-processing workflow is shown in Extended Data Fig. 3. For Rho*-GRK1(SSE/EE)–Fab1 or Rho*-GRK1(SSE/EE)–Fab6 complexes, heterogenous refinement with three classes was performed to select the class with resolvable secondary structure features in cryoSPARC⁶⁵. The selected particles were used for homogenous refinement, followed by non-uniform refinement, converging at about 4 Å global resolution, as determined by the FSC criterion in cryoSPARC⁶⁵. The data-processing workflows are shown in Extended Data Figs. 4 and 5, respectively. Directional FSC was performed by an online 3DFSC server to evaluate the resolution in different directions⁶⁶. A number of factors prevented further improvement of the current resolution, including the small size and intrinsic flexibility of the complex, as well as preferred orientations.

PC analysis

PC analysis of GRK kinase domain conformations^{30,67} was recalculated on the basis of an updated dataset, as follows. Four GRK2 structures published since the last analysis (PDB entries 5UVC, 5UUU, 6C2Y, and 6U7C) were added to the previous PKA (201 structures) and GRK (59 structures) dataset, and the kinase domains of the structures were aligned using the structurally invariant core residues identified previously³⁰. PCs were calculated using equivalent kinase domain Cα atoms of all structures excluding the new Rho*-bound GRK1 structures generated by MDFF and the recent GRK5–Ca²⁺·CaM structure PDB entry 6PJX. All structures (including the new models and 6PJX) were then projected into the subspace spanned by the two PCs that captured the largest structural variance (that is, PC1 and PC2, which in total capture 77.2% of total variance) for inter-structure comparisons. Each PC axis represents a linear combination of Cartesian coordinates (in Å), where the origin represents the mean conformation of all structures used to compute PCs.

Negative-stain EM

For negative-stain EM, 4 µl of Rho*-GRK1 complex was added to a glow discharged 400-mesh copper grid covered with carbon-coated collodion film (EMS). Grids were washed in one drop of water, stained in three drops of uranyl formate (0.7%) (EMS) and air dried. Samples were visualized on a Tecnai T12 electron microscope (FEI) at an acceleration voltage of 120 kV under low-dose conditions. Images were taken at a magnification of 71,138 \times at a defocus value of $-1.4\text{ }\mu\text{m}$ and recorded on a Gatan US4000 CCD camera (Gatan). Images were converted to mixed raster content format and binned (2×2 pixels), resulting in final images with a pixel size of 4.16 \AA/pixel at the specimen level. A total of 18,227 particle projections were excised using Boxer (part of the EMAN 2.1 software suite)⁶⁸ from 80 micrographs. Boxed out particle projections were subjected to 2D reference-free alignment and classification using ISAC⁶⁹. The particles from ISAC 2D classification were further cleaned using RELION⁶² and resulted in 29 good class averages with 15,056 particle projections.

Reporting summary

Further information on research design is available in the Nature Research Reporting Summary linked to this paper.

Data availability

All data needed to evaluate the conclusions in the paper are presented in the paper and/or the Supplementary Materials. Additional data related to this paper are available upon reasonable request from the authors. The structures of the four Rho*-GRK1 complexes (Rho*-GRK1, Rho*-GRK1(S5E/EE), Rho*-GRK1(S5E/EE)-Fab1, and Rho*-GRK1(S5E/EE)-Fab6) and their associated data have been deposited into the Protein Data Bank under accession codes 7MT9, 7MT8, 7MTA, and 7MTB, and the Electron Microscopy Data Bank under accession codes EMD-23978, EMD-23977, EMD-23979, and EMD-23980, respectively. CLMS data have been deposited to the ProteomeXchange Database (<http://www.proteomexchange.org/>) via the PRIDE⁷⁰ partner repository with dataset identifier PXDO19215.

52. Yu, Q. M. et al. The amino terminus with a conserved glutamic acid of G protein-coupled receptor kinases is indispensable for their ability to phosphorylate photoactivated rhodopsin. *J. Neurochem.* **73**, 1222–1227 (1999).
53. Sterne-Marr, R. et al. GRK2 activation by receptors: role of the kinase large lobe and carboxyl-terminal tail. *Biochemistry* **48**, 4285–4293 (2009).
54. Komolov, K. E., Bhardwaj, A. & Benovic, J. L. Atomic structure of GRK5 reveals distinct structural features novel for G protein-coupled receptor kinases. *J. Biol. Chem.* **290**, 20629–20647 (2015).
55. Lodowski, D. T. et al. The role of G $\beta\gamma$ and domain interfaces in the activation of G protein-coupled receptor kinase 2. *Biochemistry* **44**, 6958–6970 (2005).
56. Baameur, F. et al. Role for the regulator of G-protein signaling homology domain of G protein-coupled receptor kinases 5 and 6 in $\beta 2$ -adrenergic receptor and rhodopsin phosphorylation. *Mol. Pharmacol.* **77**, 405–415 (2010).

57. Lodowski, D. T., Tesmer, V. M., Benovic, J. L. & Tesmer, J. J. The structure of G protein-coupled receptor kinase (GRK)-6 defines a second lineage of GRKs. *J. Biol. Chem.* **281**, 16785–16793 (2006).
58. Papermaster, D. S. Preparation of retinal rod outer segments. *Methods Enzymol.* **81**, 48–52 (1982).
59. Paduch, M. et al. Generating conformation-specific synthetic antibodies to trap proteins in selected functional states. *Methods* **60**, 3–14 (2013).
60. Miller, K. R. et al. T cell receptor-like recognition of tumor *in vivo* by synthetic antibody fragment. *PLoS ONE* **7**, e43746 (2012).
61. Suloway, C. et al. Automated molecular microscopy: the new Leginon system. *J. Struct. Biol.* **151**, 41–60 (2005).
62. Zivanov, J. et al. New tools for automated high-resolution cryo-EM structure determination in RELION-3. *eLife* **7**, e42166 (2018).
63. Zheng, S. Q. et al. MotionCor2: anisotropic correction of beam-induced motion for improved cryo-electron microscopy. *Nat. Methods* **14**, 331–332 (2017).
64. Zhang, K. Gctf: real-time CTF determination and correction. *J. Struct. Biol.* **193**, 1–12 (2016).
65. Punjani, A., Rubinstein, J. L., Fleet, D. J. & Brubaker, M. A. cryoSPARC: algorithms for rapid unsupervised cryo-EM structure determination. *Nat. Methods* **14**, 290–296 (2017).
66. Tan, Y. Z. et al. Addressing preferred specimen orientation in single-particle cryo-EM through tilting. *Nat. Methods* **14**, 793–796 (2017).
67. Bouley, R. et al. Structural determinants influencing the potency and selectivity of indazole-paroxetine hybrid G protein-coupled receptor kinase 2 inhibitors. *Mol. Pharmacol.* **92**, 707–717 (2017).
68. Ludtke, S. J., Baldwin, P. R. & Chiu, W. EMAN: semiautomated software for high-resolution single-particle reconstructions. *J. Struct. Biol.* **128**, 82–97 (1999).
69. Yang, Z., Fang, J., Chittuluru, J., Asturias, F. J. & Penczek, P. A. Iterative stable alignment and clustering of 2D transmission electron microscope images. *Structure* **20**, 237–247 (2012).
70. Perez-Riverol, Y. et al. The PRIDE database and related tools and resources in 2019: improving support for quantification data. *Nucleic Acids Res.* **47**, D442–D450 (2019).
71. Rasmussen, S. G. et al. Crystal structure of the $\beta 2$ adrenergic receptor-Gs protein complex. *Nature* **477**, 549–555 (2011).
72. Bujacz, A. Structures of bovine, equine and leporine serum albumin. *Acta Crystallogr. D* **68**, 1278–1289 (2012).
73. Combe, C. W., Fischer, L. & Rappaport, J. xiNET: cross-link network maps with residue resolution. *Mol. Cell. Proteomics* **14**, 1137–1147 (2015).

Acknowledgements This work was supported by National Institutes of Health grants HL071818, HL122416, and CA221289 (to J.J.G.T.), GM117372 (to A.A.K.), GM095832, GM105942, GM109896, and GM105920 (to P.C.A.), an American Heart Association Post-Doctoral Fellowship (19POST34450193, to Q.C.), and National Science Foundation grant MCB-1517617 (to X.-Q.Y.). J.J.G.T. was also supported by the Walther Cancer Foundation. We thank the Purdue Cryo-EM Facility for equipment access and support.

Author contributions Q.C. and J.J.G.T. conceptualized the study. Q.C. produced and purified rhodopsin and GRK1, and performed crosslinking and kinetic assays. S.M., Q.C., J.J.G.T., and A.A.K. selected the Fabs. Q.C., J.J.G.T., Z.L., and L.C. collected data and performed structure determinations of Rho*-GRK1 and Rho*-GRK1(S5E/EE). Q.C. and J.J.G.T. collected data and performed structure determinations of Rho*-GRK1(S5E/EE)-Fab1 and Rho*-GRK1(S5E/EE)-Fab6. T.K. assisted with cryo-EM data collection for all four reconstructions. M.P. and P.C.A. performed the mass spectrometry analysis. D.P. collected and performed negative-stain EM analysis. C.-L.C., J.J.G.T. and Q.C. performed docking and molecular simulations. X.-Q.Y. performed the PCA analysis. Q.C. wrote the original draft and all authors further edited the manuscript. Q.C., J.J.G.T. and P.C.A. contributed funding.

Competing interests The authors declare no competing interests.

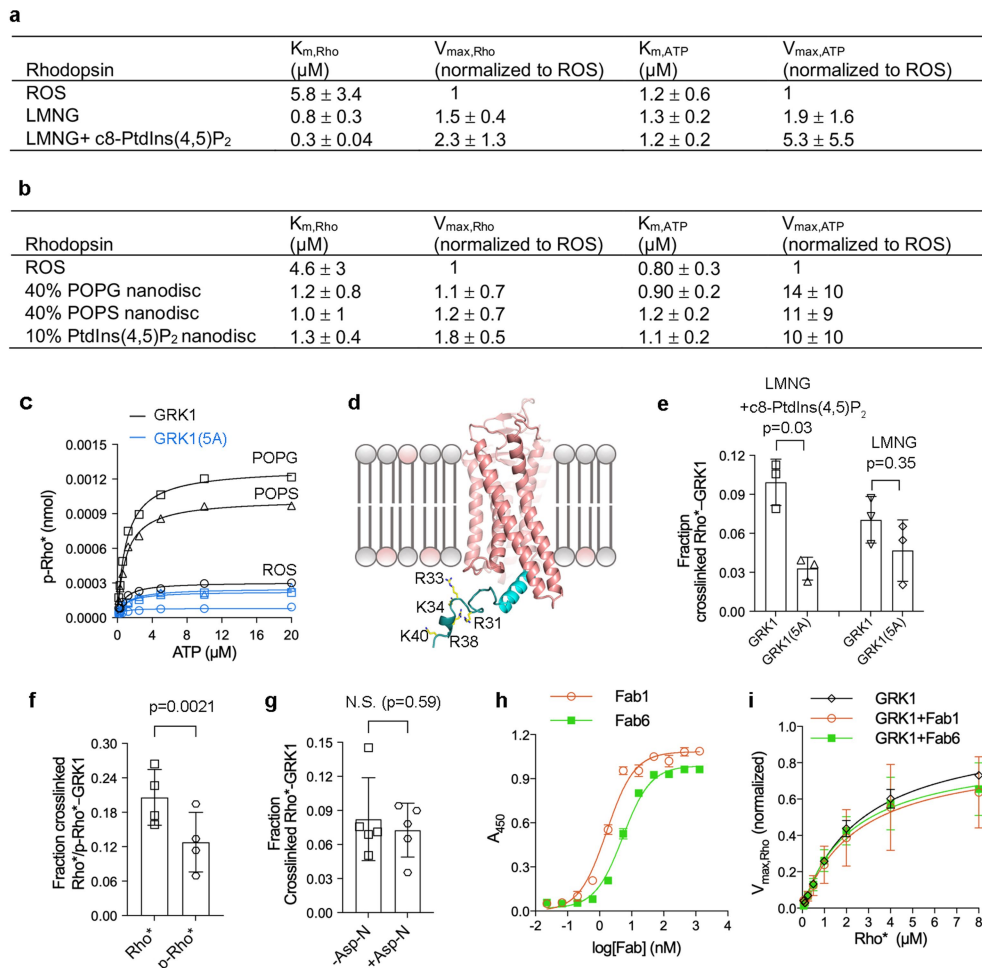
Additional information

Supplementary information The online version contains supplementary material available at <https://doi.org/10.1038/s41586-021-03721-x>.

Correspondence and requests for materials should be addressed to J.J.G.T.

Peer review information *Nature* thanks Vsevolod Gurevich, Carol Robinson and Patrick M. Sexton for their contribution to the peer review of this work.

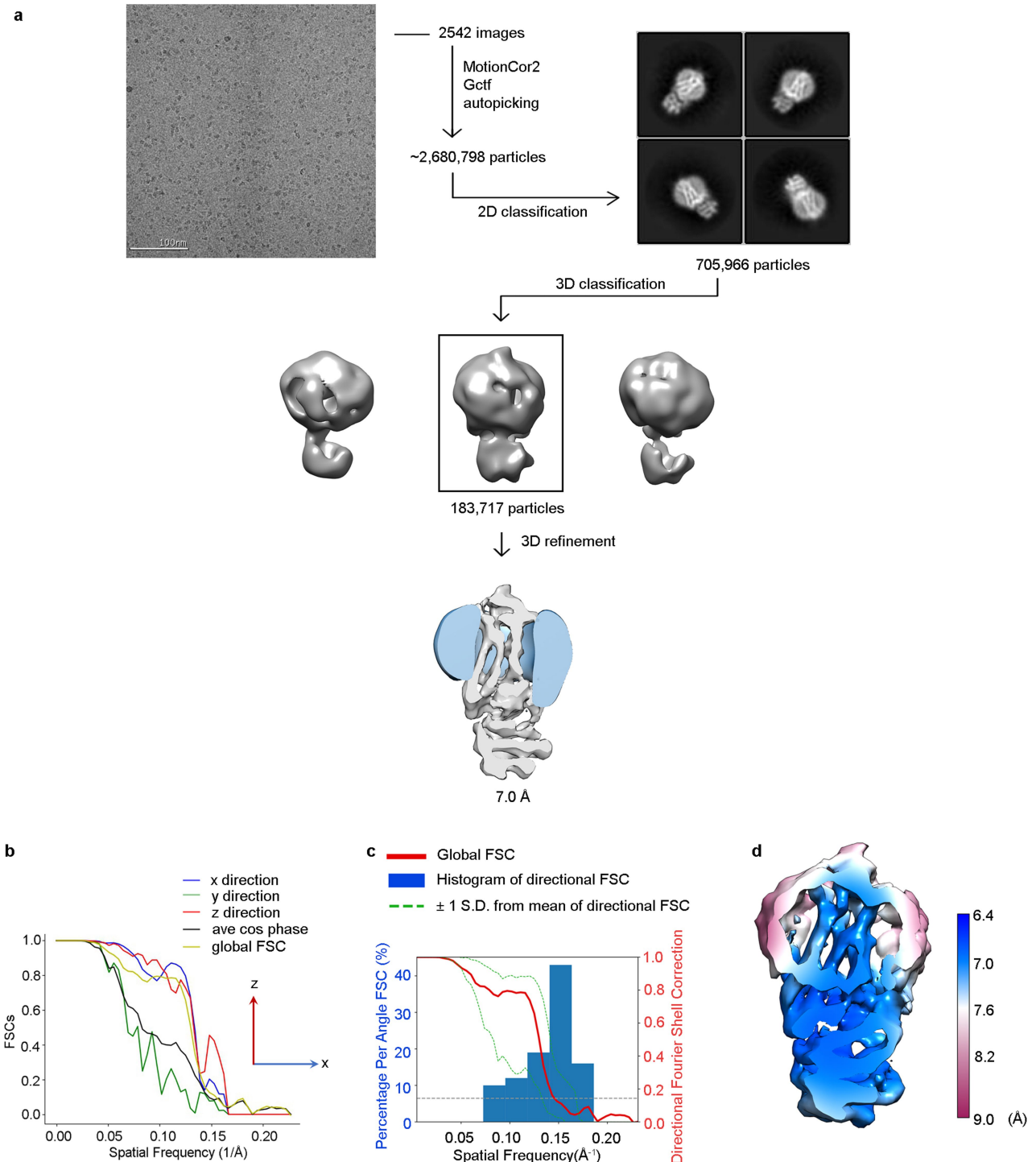
Reprints and permissions information is available at <http://www.nature.com/reprints>.



Extended Data Fig. 1 | Modulation of GRK1 activity by anionic lipids, Rho* C-terminal modifications, and Fab fragments. **a**, Kinetic analysis of GRK1 phosphorylation of Rho* in ROS or LMNG or LMNG + c8-PtdIns(4,5)P₂. Mean \pm s.d., $n = 4$ technical replicates. Reactions were performed in 50 mM HEPES (pH 8.0), 10 mM MgCl₂ for 2 min at room temperature. **b**, Kinetic analysis of GRK1 phosphorylation of Rho* in ROS or POPC nanodiscs containing 40% POPG or 40% POPS or 10% PtdIns(4,5)P₂. Mean \pm s.d., $n = 3$ technical replicates. Reactions were performed in 50 mM HEPES (pH 8.0), 10 mM MgCl₂ for 2 min at room temperature. **c**, Representative Michaelis–Menten kinetics measurement with varying ATP. Rho* was reconstituted with POPC nanodiscs containing 40% POPG (black squares) or 40% POPS (black triangles) and compared with Rho* in ROS (black circles). GRK1(5A) activity was greatly diminished relative to GRK1 under these conditions (blue symbols) but was still somewhat responsive to anionic lipids. **d**, Approximate location of the five positively charged residues places them close to the lipid bilayer. **e**, The crosslinking yield (corresponding to the amount of complex formed divided by the sum of the input GRK1 and Rho*) of GRK1(5A) was significantly lower than that of GRK1 in the presence of c8-PtdIns(4,5)P₂ but not in its absence. The

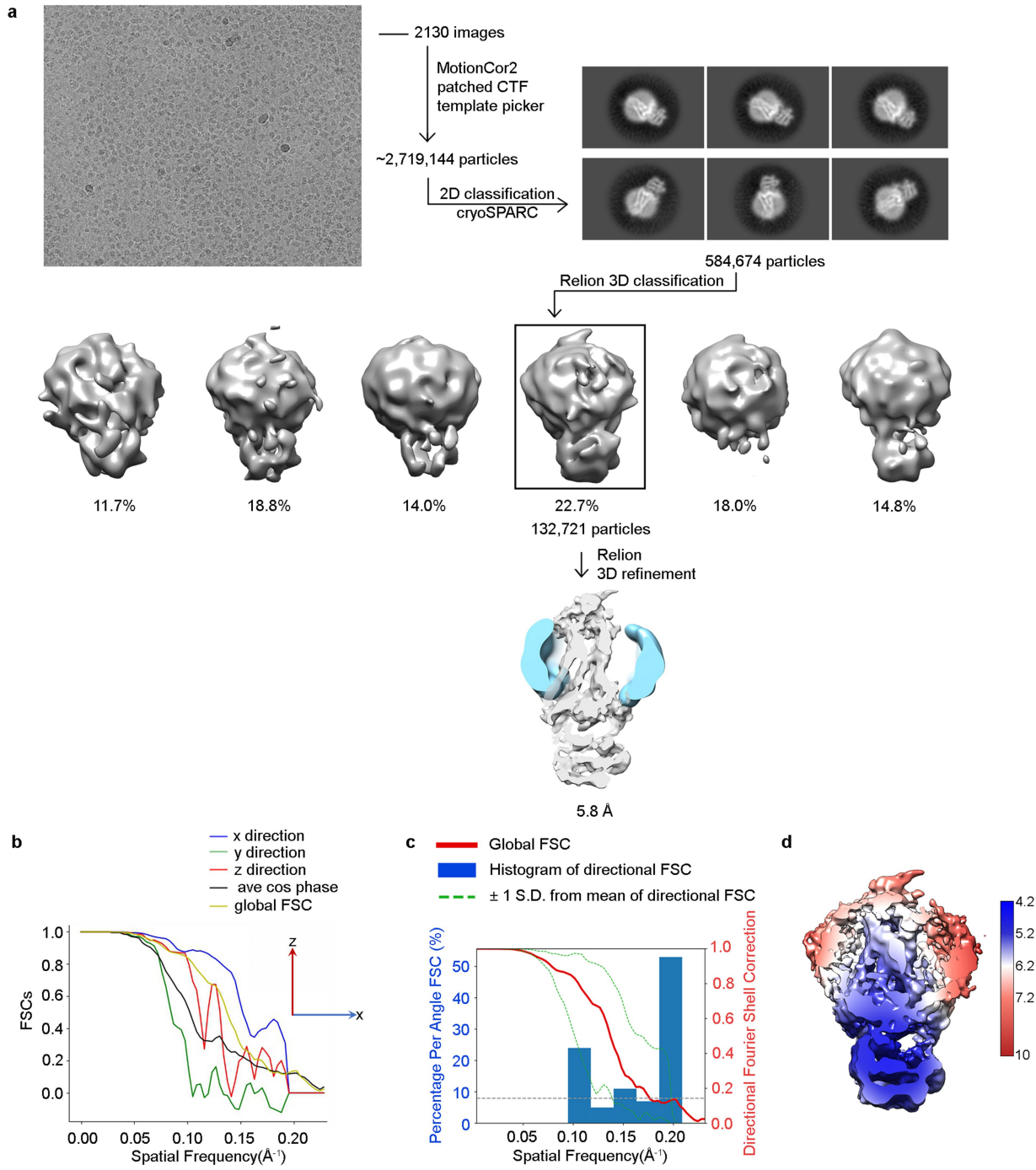
crosslinking level of GRK1(5A) was compared with that of GRK1 using a two-sided *t*-test ($n = 3$ technical replicates) in the presence or absence of c8-PtdIns(4,5)P₂. For gel source data, see Supplementary Fig. 5f. **f**, The crosslinking yield of p-Rho* (with estimated 6–8 phosphates out of 7 incorporated based on a standard curve) with GRK1 was compared with that of unphosphorylated rhodopsin using two-sided *t*-test ($n = 4$ technical replicates). For gel source data, see Supplementary Fig. 5h. **g**, The crosslinking yield of Asp-N-truncated Rho* (cleavage site N-terminal to Asp329) was compared with that of full-length Rho* using two-sided *t*-test ($n = 5$ technical replicates; N.S., not significant). For gel source data, see Supplementary Fig. 5i. The GRK1(K479R) mutant, which eliminates the other prominent crosslinking site, also did not affect our ability to trap the complex (data not shown). Mean \pm s.d. **h**, ELISA analysis of Fab1 and Fab6 binding to GRK1 yielded EC₅₀ values of 2 and 5 nM, respectively ($n = 3$ technical replicates). Mean \pm s.d. **i**, Michaelis–Menten analysis of GRK1 in the absence or presence of threefold molar excess Fab1 or Fab6 ($n = 3$ technical replicates). Data were normalized to the fit $V_{max, \text{Rho}}$ of GRK1. Mean \pm s.d.

Article



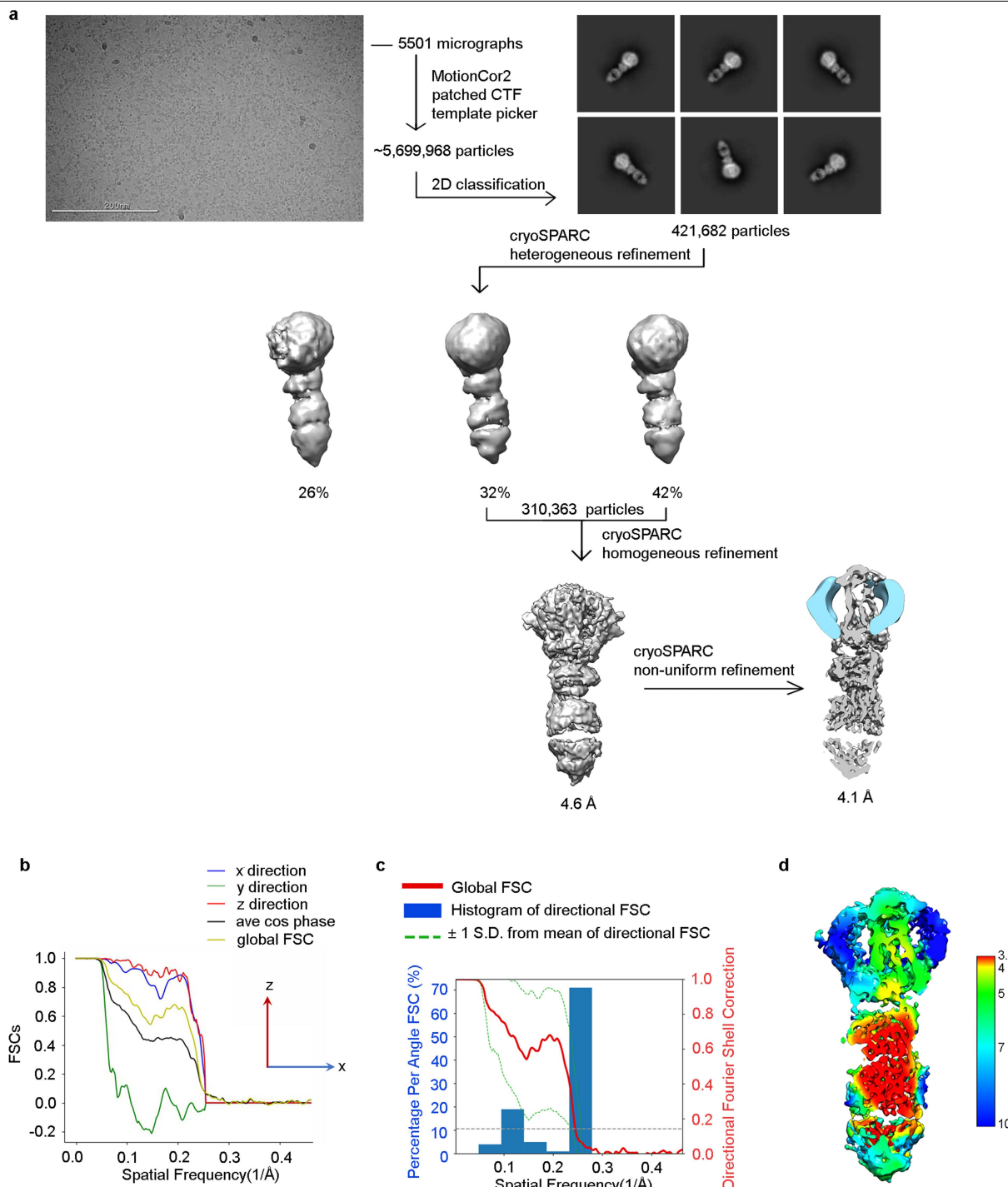
Extended Data Fig. 2 | Workflow of cryo-EM data processing and resolution analysis of Rho*-GRK1. **a**, Representative raw cryo-EM micrograph from a total of 2,542. From these, 2.7 million particles were automatically picked in RELION-3 and were used to generate 2D class averages (shown are representative good classes). After screening out bad classes, 705,966 particles remained. Three major classes from 3D classification were generated in RELION-3 using an initial model generated by cryoSPARC. Class 2 (183,717 particles) showed the best quality and was selected for 3D auto-refinement, resulting in a final map at

a global resolution of 7.0 Å (FSC cut-off = 0.143). **b**, Directional FSC indicated that the resolutions in the *x* and *z* directions are similar to the global resolution, whereas the resolution in the *y* direction is lower because fewer particles have this axis resolved. **c**, Plots of the global FSC together with the spread of directional resolution values defined by $\pm 1\sigma$ from the mean and a histogram of 100 such values evenly sampled over the 3D FSC. **d**, Local resolution map as estimated by RELION-3.



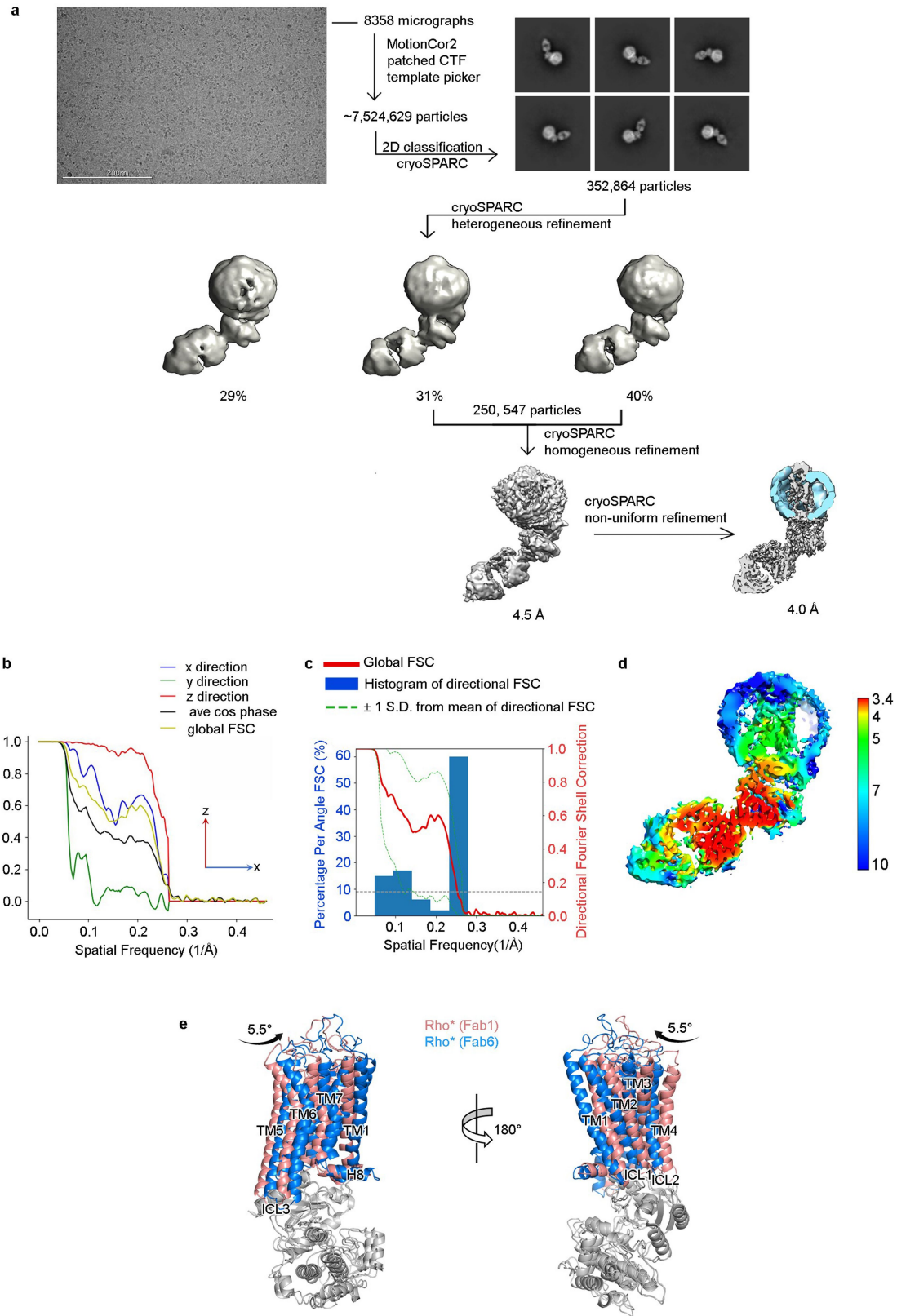
Extended Data Fig. 3 | Workflow of cryo-EM data processing and resolution analysis of Rho*-GRK1(SSE/EE). **a**, Representative raw cryo-EM micrograph from a total of 2,130. From these, 2.7 million particles were automatically picked in cryoSPARC and were used to generate 2D class averages (shown are representative good classes). After screening out bad classes, the 584,674 remaining particles were imported to RELION-3 and used to generate six major classes from 3D classification in RELION-3 using an initial model generated by cryoSPARC. Class 6 (132,721 particles) showed the best quality and was selected

for 3D auto-refinement, resulting in a final map at a global resolution of 5.8 Å (FSC cut-off = 0.143). **b**, Directional FSC indicates that the resolutions in the x and z directions are similar to the global resolution, whereas the resolution in the y direction is lower. **c**, Plots of the global FSC together with the spread of directional resolution values defined by $\pm 1\sigma$ from the mean and a histogram of 100 such values evenly sampled over the 3D FSC. **d**, Local resolution map as estimated by RELION-3.



Extended Data Fig. 4 | Workflow of cryo-EM data processing and resolution analysis of Rho*-GRK1(SSE/EE)-Fab1. **a**, Representative raw cryo-EM micrograph from a total of 5,501. From these, 5.7 million particles were automatically picked in cryoSPARC and were used to generate 2D class averages (shown are representative good classes). After screening out bad classes, the 421,682 remaining particles were further processed using heterogeneous refinement. Classes 2 and 3 showed similar quality and were selected for homogeneous refinement and then non-uniform refinement in

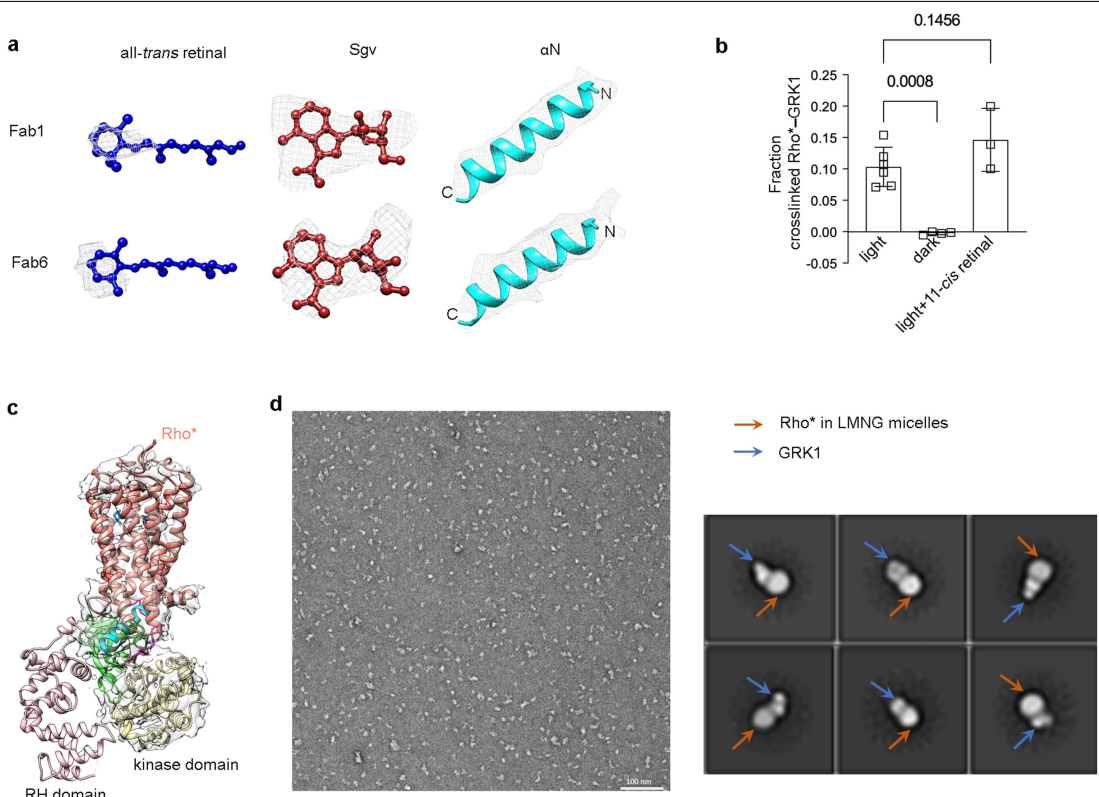
cryoSPARC, resulting in a final map at a global resolution of 4.1 Å (FSC cut-off = 0.143). **b**, Directional FSC indicates that the resolutions in the x and z directions are similar to the global resolution, whereas the resolution in the y direction is lower. **c**, Plots of the global FSC together with the spread of directional resolution values defined by $\pm 1\sigma$ from the mean and a histogram of 100 such values evenly sampled over the 3D FSC. **d**, Local resolution map as estimated by cryoSPARC.



Extended Data Fig. 5 | See next page for caption.

Article

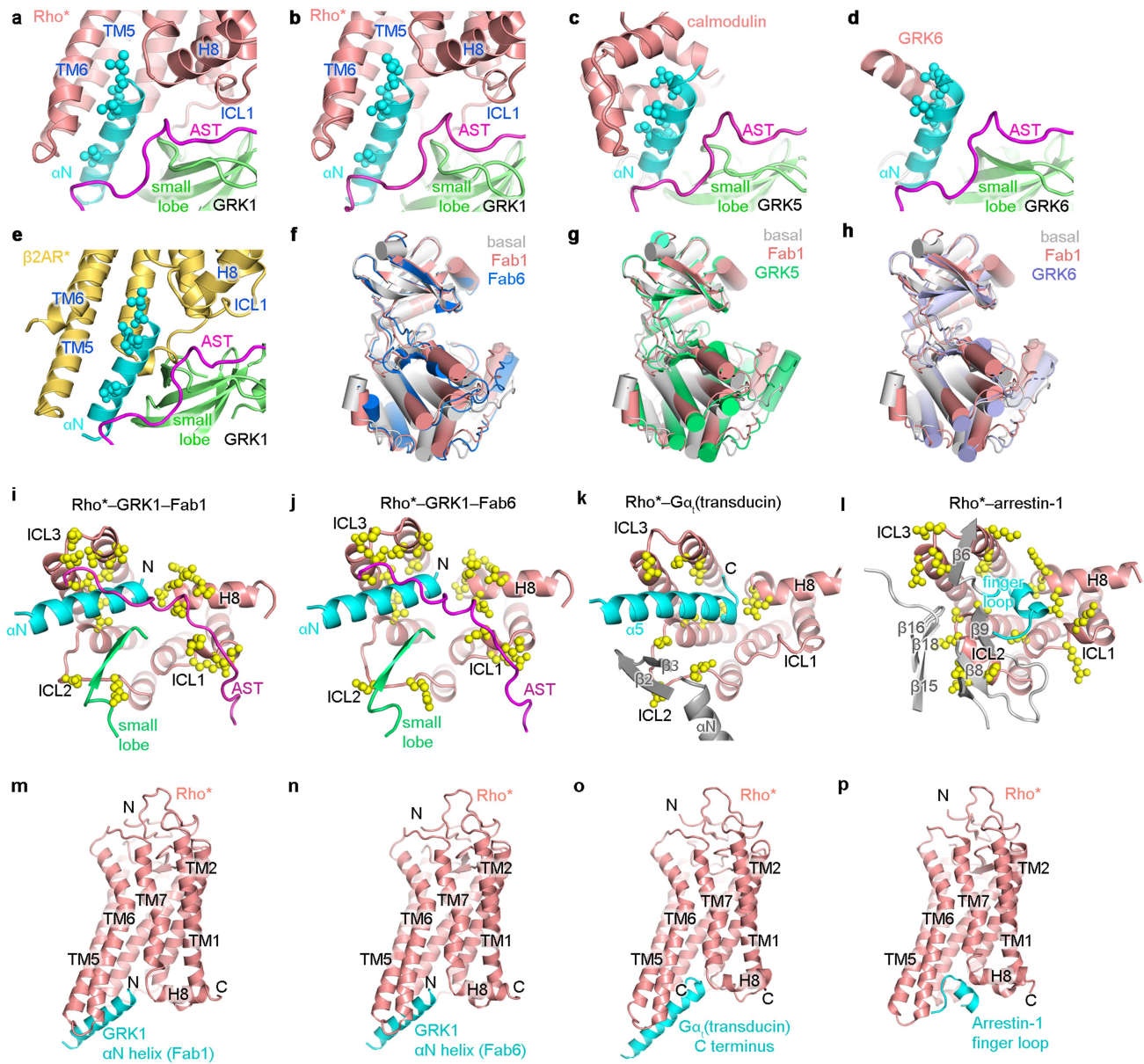
Extended Data Fig. 5 | Flow chart of cryo-EM data processing and resolution analysis of Rho*-GRK1(S5E/EE)-Fab6, and comparison of the Fab1 and Fab6 complexes. **a**, A representative raw cryo-EM micrograph from a total of 8,358. From these, 7.5 million particles were automatically picked in cryoSPARC and were used to generate 2D class averages (shown are representative good classes). After screening out bad classes, the 352,864 remaining particles were further processed using heterogeneous refinement. Classes 2 and 3 showed similar quality and were selected for homogeneous refinement and then non-uniform refinement in cryoSPARC. The resolution of the final map is estimated to be 4.0 Å. Global resolution was determined by FSC with a cut-off of 0.143. **b**, Directional FSC indicates that the resolutions in the *x* and *z* directions are similar to the globular resolution, whereas the resolution in the *y* direction is lower. **c**, Plots of the global FSC together with the spread of directional resolution values defined by $\pm 1\sigma$ from the mean and a histogram of 100 such values evenly sampled over the 3D FSC. **d**, Local resolution map as estimated by cryoSPARC. **e**, Overlay of Rho* from the Fab1 (red) and Fab6 (blue) complexes after alignment of the small lobes of their kinase domains. Rho* pivots by about 5.5°, largely around an axis roughly parallel to a vector joining the ICL1 and ICL3 loops of the receptor. The key interactions between Rho* and GRK1, namely that of TM3, TM5 and TM6 with α N, and ICL1 with the C-terminal end of the AST, stay intact. This is because the α N helix and the N-terminal half of the AST loop region of GRK1 shift with the receptor, which is reasonable given that these elements are known to be dynamic from crystal structures of GRKs. Motion of these elements is likely to be responsible for the observed difference in kinase domain conformation exhibited by the Fab1 and Fab6 complexes because they directly affect the hinge region of the kinase domain. There are, however, small conformational differences at the end of TM1 and the beginning of the ICL1 loop in Rho* that probably occur because the bound GPCR is trying to maintain optimal interactions with phosphosites at the end of the AST in each state. The conformation of ICL2 is also likely to change between the structures, but this region could not be accurately modelled. Because our PC analysis (Fig. 2e) suggests that the Fab6 complex features a less active conformation of the GRK1 kinase domain, it may represent an intermediate state in which α N and AST have engaged the receptor, but the kinase domain has yet to fully adopt a transition state-like conformation.



Extended Data Fig. 6 | Assessment of ligand density, of the presence of all-trans retinal, and of the conformational heterogeneity of the GRK1 RH domain. **a**, Electron density of all-trans retinal, contoured at 17σ (Fab1 map) and 13σ (Fab6 map); Sgv, contoured at 24σ (Fab1 map) and 26σ (Fab6 map); and α N, contoured at 21σ (Fab1 map) and 25σ (Fab6 map). **b**, Light- and GRK1 ligand-dependence of the crosslinking reaction between rhodopsin and GRK1. 11-cis retinal undergoes isomerization upon light exposure to all-trans retinal, which serves as a full agonist for rhodopsin. The crosslinking level of GRK1 with rhodopsin in the dark ($n=4$ technical replicates) and in the light with excess

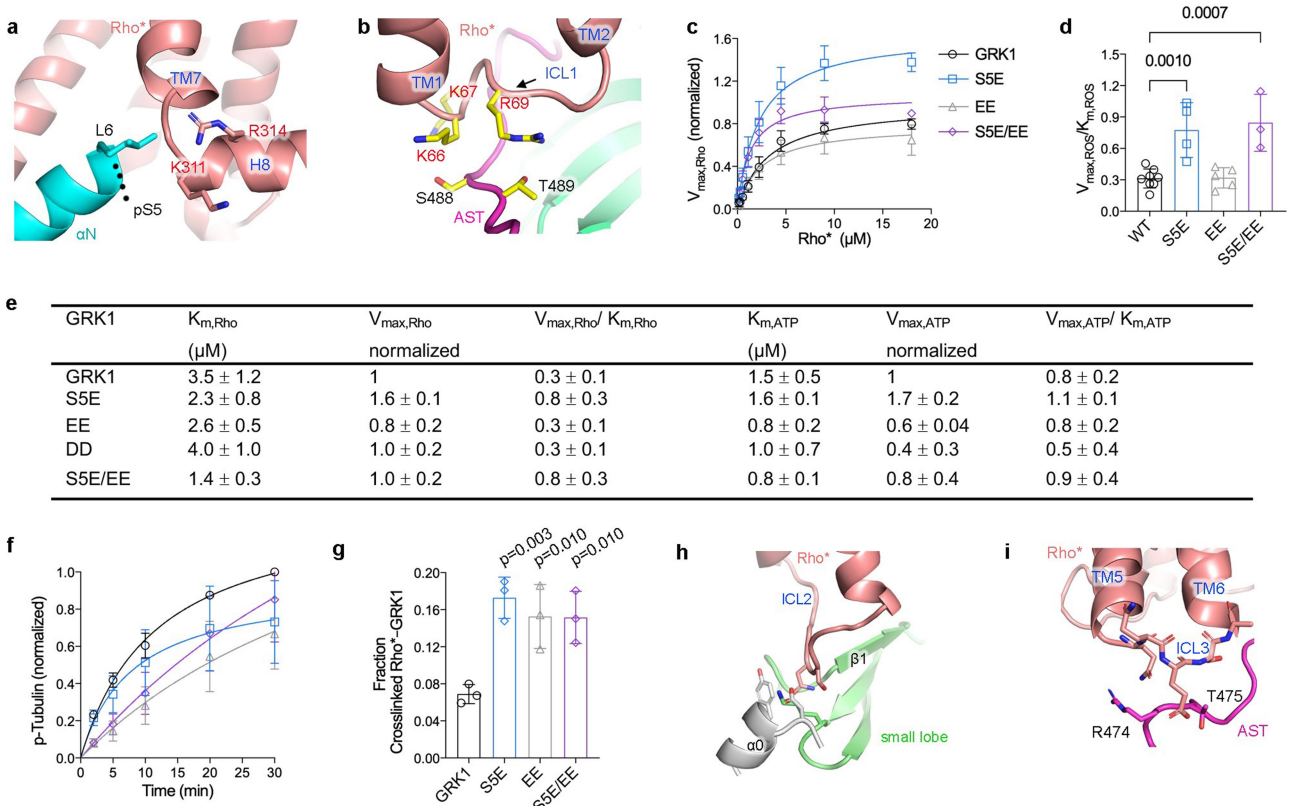
11-cis retinal ($n=3$ technical replicates) were compared to that of GRK1 with rhodopsin in the light using one-way ANOVA followed by a Dunnett's multiple comparisons test. Mean \pm s.d. **c**, Density for the RH domain was not observed by cryo-EM in any of our reconstructions. The map of Rho*-GRK1(SSE/EE)-Fab1 is shown here as an example. **d**, A representative negative-stain EM micrograph of the Rho*-GRK1 complex solubilized in LMNG (left) along with representative 2D averages (right), indicating heterogeneity in the bound GRK1. The smaller, variably positioned domain is interpreted as the RH domain.

Article



Extended Data Fig. 7 | GRK α N interactions, kinase domain conformational changes, and comparison of the interactions between Rho* and its three principal downstream targets. **a–d**, The GRK N terminus folds into a helix (α N) that packs against the small lobe and AST of the kinase domain, forming a docking side for Rho* (**a**, **b**; GRK1 with Fab1 and Fab6 complexes, respectively), Ca²⁺:CaM (**c**; GRK5 in PDB entry 6PJX²⁷), or a twofold related crystal lattice contact (**d**; GRK6 in PDB entry 3NYN⁶). The interfaces shown are mediated by the same highly conserved hydrophobic residues (side chains shown with spheres). **e**, The cytoplasmic cleft and ICL1 of activated β_2 AR in its G-protein-bound conformation (PDB entry 3SN6²¹) readily accommodates α N

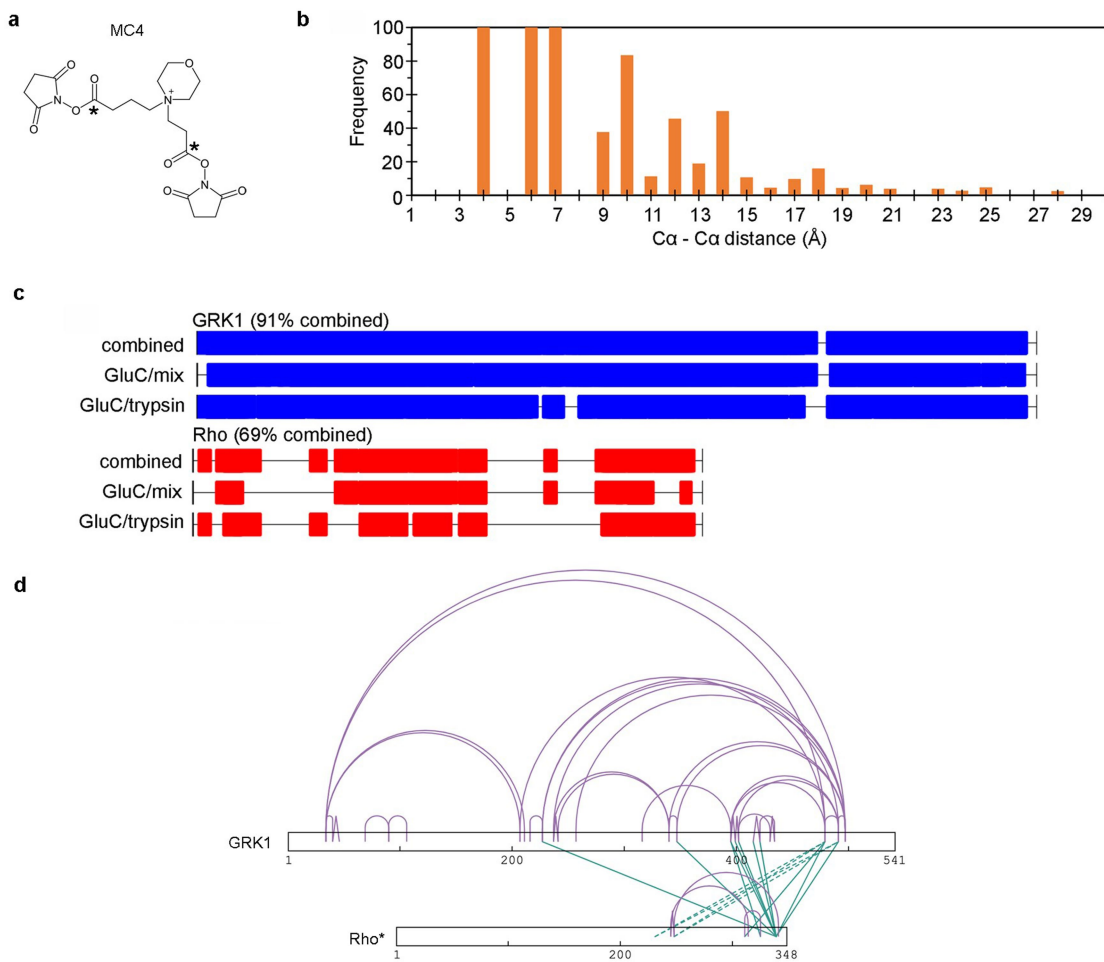
and AST of GRK1. **f–h**, Kinase domain small lobes from different ‘active’ GRK structures were aligned to highlight differences in closure. **i–l**, Comparison of downstream proteins bound to the cytoplasmic surface of Rho*. The side chains of residues interacting with GRK1 in the Fab1 complex (**i**; PDB entry 7MTA), GRK1 in the Fab6 complex (**j**; PDB entry 7MTB), G α_t (transducin) (**k**; PDB entry 6OYA¹⁴) and arrestin-1 (**l**; PDB entry 5WOP³¹) are shown as yellow spheres. Note that α N of GRK1 and α 5 of G α bind with opposite polarity. **m**, **n**, Cartoon representations of GRK1 α N helix docked to Rho* in the Fab1 (**m**) and Fab6 (**n**) models. **o**, G α_t C terminus bound to Rho* (PDB entry 6OYA¹⁴). **p**, Arrestin-1 finger loop bound to Rho* (PDB entry 5WOP³¹).



Extended Data Fig. 8 | Interactions of GRK1 with intracellular loops of Rho* and development of autophosphorylation mimetic variants. **a**, Interactions of GRK1 α N with the cytoplasmic cleft and H8 of Rho*. GRK1-Ser5 was modelled in a phosphorylated state to demonstrate proximity to Rho*-Lys311 and Arg314. **b**, GRK1AST interaction with ICL1. The key participating residues are shown with stick side chains. Ser488 and Thr489 are autophosphorylation sites in GRK1. **c–g**, Kinetic and crosslinking analysis of GRK1 and phosphomimetic mutants of Rho* autophosphorylation (SSE; S488E and T489E (EE); S488D and T489D (DD); S5E, S488E, and T489E (S5E/EE)). One-way ANOVA followed by Dunnett's multiple comparison test was carried out to compare each mutant with GRK1. Reactions were performed in 50 mM HEPES (pH 8.0), 10 mM MgCl₂ for 2 min at room temperature. Data were normalized to the $V_{\max, \text{Rho}}$ or $V_{\max, \text{ATP}}$ of

GRK1. For Rho kinetics: SSE, $n = 4$; EE, $n = 5$; DD, $n = 3$; S5E/EE, $n = 3$. For ATP kinetics: SSE, $n = 3$; EE, $n = 3$; DD, $n = 4$; S5E/EE, $n = 4$ (all technical replicates). All data shown as mean \pm s.d. **f**, Time courses of tubulin phosphorylation by GRK1 and variants are similar. Data were normalized to the phosphorylation level of tubulin by GRK1 at 30 min ($n = 3$ technical replicates). **g**, Crosslinking yield of GRK1 variants relative to GRK1 ($n = 3$ technical replicates). For gel source data, see Supplementary Fig. 5. **h**, Interaction of the GRK1 small lobe with ICL2 of Rho*. The GRK1 α O helix from a basal ATP-bound structure (PDB entry 3C4Z⁴⁹) is modelled by aligning its small lobe with that in the Rho*-GRK1(S5E/EE)-Fab1 complex, demonstrating a potential clash between ICL2 and α O. **i**, Interaction of GRK1AST with ICL3.

Article



Extended Data Fig. 9 | MC4 crosslinker properties and liquid chromatography tandem mass spectrometry peptide coverage of the Rho*-GRK1 complex. **a**, MC4 has two symmetrical amine-reactive NHS esters separated by a C4 linker attached to a quaternary *N*-morpholine group. *Conformational analyses of in vacuo MD simulations suggest an average carboxy C–C distance of approximately 6 Å. **b**, Characterization of MC4 reactive distance using BSA. The y-axis shows the frequency (expressed as %) of experimentally identified crosslinked lysine pairs within a certain Cα–Cα

distance (x-axis) based on a BSA crystal structure (PDB entry 4F5S⁷²). **c**, Peptide sequence coverage obtained for the purified crosslinked Rho*-GRK1 complex after multistep digestion with *Staphylococcus aureus* Protease V8 (GluC)/mix (1:1 mixture of GluC/trypsin and GluC/chymotrypsin) or GluC/trypsin.

d, Intramolecular and intermolecular crosslinks summarized from Supplementary Data Tables 2, 3 are shown with a bar plot generated by XiNET⁷³. Dashed green lines represent rare intermolecular crosslinks that were too distant to react in our cryo-EM models.

Extended Data Table 1 | GRK mutations and their effects on kinase activity towards Rho* or a soluble substrate

α N Helix		Rho*	soluble substrate	Ref
ΔN19	bGRK1	---	---	28
ΔN15	hGRK1	---	NC	52
ΔN30	hGRK1	---	NC	52
ΔN15	bGRK2	---	ND	52
ΔN30	bGRK2	---	ND	52
ΔN2-14	hGRK5	---	NC [‡]	7
D2A	hGRK1	NC	NC	52
S5E	bGRK1	+	--	1
S5A	bGRK1	--	ND	49
D3A	hGRK2	-	ND [§]	5,33
D3N	hGRK2	-	ND	33
D3K	hGRK2	---	NC	33
L6A	bGRK1	---	+	34
L4A	hGRK2	---	NC	33
L4A	hGRK2	--	+	5
L4K	hGRK2	---	ND	33
L3Q	hGRK5	---	ND	7
L3Q/K113R	hGRK5	---	NC	7
L3A	hGRK6	-	NC	6
E7A	bGRK1	---	+	34
E7A	hGRK1	---	+	52
E5A	hGRK2	-	NC	33
E5A	bGRK2	---	NC	52
E4A	hGRK6	-	-	6
T8A	bGRK1	-	ND	49
T8E	bGRK1	---	ND	49
V9A	bGRK1	---	+	34
V7E	hGRK2	--	+	5
I6A	hGRK6	---	NC	6
V10A	bGRK1	---	+	34
V7A	hGRK6	---	NC	6
L7A/V8A	hGRK2	---	ND	33
I6A/V7A	hGRK6	---	NC	6
I6E/V7E	hGRK6	---	NC	6
A11E	bGRK1	-	-	34
N12A	bGRK1	---	---	34
D10A	hGRK2	---	NC	5,33
D10A	hGRK2	-	-	5
D10R	hGRK2	---	-	5
N9A	hGRK6	---	--	6
T10P	hGRK5	--	NC	7
F15A	bGRK1	----	----	34
Y13A	hGRK2	--	-	5
L12A	hGRK6	---	--	6
I16A	bGRK1	--	--	34
L13A	hGRK6	--	--	6
M15A	hGRK2	NC	+	5
A18E	bGRK1	--	--	34
A16V	hGRK2	NC	-	5
M17A	hGRK2	-	-	5
E18A	hGRK2	+	ND	5
AST region		Rho*	soluble substrate	Ref
P473A	bGRK2	NC	ND	53
P473E	bGRK2	-	-	53
R474A	hGRK2	NC	ND	5
R470A	bGRK5	-	ND	54
G475I	hGRK2	--	--	5
E476K	bGRK2	NC	ND	53
V476A	bGRK1	----	---	28
V477D	bGRK2	--	-	53
N478A	hGRK2	NC	ND	5
A479S	hGRK2	NC	ND	5
A480S	hGRK2	NC	ND	5
N480A	bGRK1	+	ND	28
D481A	bGRK2	NC	ND	53
A482I	hGRK2	-	ND	5
Q482A	bGRK1	+	ND	28
F483A	bGRK2	NC	ND	53
D483A	bGRK1	-	ND	28
D484A	bGRK2	NC	ND	53
V484A	bGRK1	----	----	28
I485A	bGRK2	-	-	53
F487A	bGRK1	-	ND	28
F488D	bGRK2	NC	ND	53
S488E/T489E	bGRK1	NC	-	1
S488D/T489D	bGRK1	-	-	1
S5E/S488E/T489E	bGRK1	+	NC	1
E490K	bGRK2	NC	ND	53
G495A	bGRK2	NC	ND	53
L499D	bGRK2	NC	ND	53

Small lobe	Rho*	soluble substrate	Ref
F190A	bGRK1	---	---
F190Y	bGRK1	NC	ND
F190H	bGRK1	+	ND
R191A	bGRK1	---	---
R191K	bGRK1	---	---
R195A	bGRK2	---	ND
R190A	hGRK6	---	ND
V192A	bGRK1	NC	ND
R195A	bGRK1	-	ND
Q205A	bGRK1	+	ND
G210E	bGRK1	--	ND
L212A	bGRK1	---	---
L212M	bGRK1	+	ND
N268A	bGRK1	NC	ND

Large lobe	Rho*	soluble substrate	Ref
H280A	bGRK2	NC	ND
Y274A	bGRK1	---	---
Y274F	bGRK1	+	ND
Y281A	bGRK2	-	-
H275A	bGRK1	+	ND
S284A	bGRK2	NC	ND
Q285A	bGRK2	NC	ND
Q285K	bGRK2	NC	ND
K395A	bGRK2	NC	ND
K397A	bGRK2	NC	ND

RH domain	Rho*	soluble substrate	Ref
R31A/R33A/K34A/R38A/K40A	bGRK1	---	ND [¶]
K46L	hGRK1	NC	ND
Q41L	hGRK5	NC	ND
D164A	bGRK1	-	ND
L166K	bGRK1	-	ND
D164A/L166K	bGRK1	-	ND
L33N	hGRK2	NC	NC
E36A	hGRK2	NC	NC
V42E	bGRK2	--	ND
Y46A	bGRK2	-	ND
R68A	hGRK5	+	ND
P61A/Q69A	hGRK5	=	ND
L66A/H38A	hGRK5	---	ND
L66A/P73A	hGRK5	---	ND
L66A/E514A	hGRK5	---	ND
L66A/P37A	hGRK5	---	ND
L66A/R69A	hGRK6	--	ND
L66A/Q172A	hGRK6	---	ND
F166A/H38A	hGRK5	---	ND
F166A/E514A	hGRK5	---	ND
F166A/P61A	hGRK5	---	-
F166A/L66A	hGRK5	---	-
Y166A/L66A	hGRK6	---	ND
F166A/Q172A	hGRK5	---	ND
Y166A/Q172A	hGRK6	---	ND
Y166A/L176A	hGRK6	---	ND
F166A/W173A	hGRK5	---	-
Q172A/W173A	hGRK6	---	ND
E96A	bGRK2	NC	ND
R516A	bGRK2	NC	ND
E520A	bGRK2	--	ND
E532A	bGRK2	NC	NC
L536N	hGRK2	NC	NC
L547N	hGRK2	NC	NC
P638D	hGRK2	--	ND
V92A	hGRK5	ND	NC
V92L	hGRK5	ND	NC
V92M	hGRK5	ND	NC
K454A	hGRK5	ND	NC
R455A	hGRK5	ND	NC
K454A/R455A	hGRK5	ND	NC
I39E/I165E	hGRK6	NC	ND
I165E/F527D	hGRK6	NC	ND

Data from refs. ^{24-72,33,34,49,52-57}. h and b denote human and bovine GRKs, respectively.

^{*}--- (red), >100-fold reduction; ----, 20–100-fold reduction; ---, 10–20-fold reduction; --, 5–10-fold reduction; -, 3–5-fold reduction.

[†]NC, no change.

[‡]ND, not determined.

^{||}+, 1–3-fold increase.

[¶]Mutation is characterized in the current paper.

Article

Extended Data Table 2 | Cryo-EM data collection, refinement, and validation statistics

	Rho*-GRK1 (ensemble1 [†])	Rho*-GRK1(S5E/EE) (ensemble1)	Fab1 (ensemble1)	Fab6 (ensemble1)
Data collection and processing				
Magnification	81,000 ×	81,000 ×	81,000 ×	81,000 ×
Voltage (kV)	300	300	300	300
Electron exposure(e-/Å ²)	~54	~54	~54	~54
Defocus range (μm)	1.2 – 2.5	1.2 – 2.5	1.2 – 2.5	1.2 – 2.5
Pixel size (Å)	1.08	1.08	1.08	1.08
Symmetry imposed	C1	C1	C1	C1
Initial particle images (no.)	2,680,798	2,719,144	5,699,968	7,524,629
Final particle images (no.)	183,717	132,721	310,363	250,547
Map resolution (Å)	7.0	5.8	4.1	4.0
FSC threshold	0.143	0.143	0.143	0.143
Map resolution range (Å)	6 – 11	4.2–11	3.6–10	3.4–10
Refinement with MDFF				
Initial model used (PDB entry)	Rho*: 3PQR; GRK1: a homology model of 3NYN, Fab models: SWISSMODEL ⁷⁴			
Model composition				
Non-hydrogen atoms	5358	5363	8699	8707
Residues	Protein: 670	Protein: 670	Protein: 1108	Protein: 1109
Ligands	Sgv: 1	Ret: 1	Sgv: 1	Ret: 1
R.m.s. deviations				
Bond lengths (Å)	0.019	0.019	0.143	0.019
Bond angles (°)	2.01	1.95	2.88	2.02
Validation				
MolProbity score	1.31	1.26	1.22	1.17
Clash score	0.48	0.48	0.24	0.18
Poor rotamers (%)	1.52	1.52	1.46	1.46
Ramachandran Plot				
Favored (%)	91.6	92.8	91.4	92.3
Allowed (%)	6.3	5.9	6.2	6.1
Disallowed (%)	2.1	1.4	2.4	1.6

[†]The ensemble most similar to all other ensembles (lowest backbone r.m.s.d. over the Rho*-GRK1 complex residues) was used to generate statistics.

Reporting Summary

Nature Research wishes to improve the reproducibility of the work that we publish. This form provides structure for consistency and transparency in reporting. For further information on Nature Research policies, see our [Editorial Policies](#) and the [Editorial Policy Checklist](#).

Statistics

For all statistical analyses, confirm that the following items are present in the figure legend, table legend, main text, or Methods section.

n/a Confirmed

- The exact sample size (n) for each experimental group/condition, given as a discrete number and unit of measurement
- A statement on whether measurements were taken from distinct samples or whether the same sample was measured repeatedly
- The statistical test(s) used AND whether they are one- or two-sided
Only common tests should be described solely by name; describe more complex techniques in the Methods section.
- A description of all covariates tested
- A description of any assumptions or corrections, such as tests of normality and adjustment for multiple comparisons
- A full description of the statistical parameters including central tendency (e.g. means) or other basic estimates (e.g. regression coefficient) AND variation (e.g. standard deviation) or associated estimates of uncertainty (e.g. confidence intervals)
- For null hypothesis testing, the test statistic (e.g. F , t , r) with confidence intervals, effect sizes, degrees of freedom and P value noted
Give P values as exact values whenever suitable.
- For Bayesian analysis, information on the choice of priors and Markov chain Monte Carlo settings
- For hierarchical and complex designs, identification of the appropriate level for tests and full reporting of outcomes
- Estimates of effect sizes (e.g. Cohen's d , Pearson's r), indicating how they were calculated

Our web collection on [statistics for biologists](#) contains articles on many of the points above.

Software and code

Policy information about [availability of computer code](#)

Data collection Leginon 3.4 was used for automated data collection on the Titan Krios.

Data analysis GraphPad Prism 9, Eman2.1, RELION 3.0, MotionCor2, Chimera 1.12, cryoSPARC v2.12.0-v3.2, PYMOL 2.3.5, Thermo Proteome Discover 2.3, MeroX 2.0b, MSFragger

For manuscripts utilizing custom algorithms or software that are central to the research but not yet described in published literature, software must be made available to editors and reviewers. We strongly encourage code deposition in a community repository (e.g. GitHub). See the Nature Research [guidelines for submitting code & software](#) for further information.

Data

Policy information about [availability of data](#)

All manuscripts must include a [data availability statement](#). This statement should provide the following information, where applicable:

- Accession codes, unique identifiers, or web links for publicly available datasets
- A list of figures that have associated raw data
- A description of any restrictions on data availability

The structures of the four Rho*-GRK1 complexes: Rho*-GRK1, Rho*-GRK1S5E/EE, Rho*-GRK1S5E/EE-Fab1, and Rho*-GRK1S5E/EE-Fab6, and their associated data have been deposited into the Protein Data Bank under accession codes 7MT9, 7MT8, 7MTA, and 7MTB, and the Electron Microscopy Data Bank under accession code EMD-23978, 23977, 23979, and 23980, respectively. CLMS data have been deposited to the ProteomeXchange Consortium via the PRIDE partner repository with dataset identifier PXD019215.

Field-specific reporting

Please select the one below that is the best fit for your research. If you are not sure, read the appropriate sections before making your selection.

Life sciences Behavioural & social sciences Ecological, evolutionary & environmental sciences

For a reference copy of the document with all sections, see nature.com/documents/nr-reporting-summary-flat.pdf

Life sciences study design

All studies must disclose on these points even when the disclosure is negative.

Sample size	Sample size calculation was not performed.
Data exclusions	No data were excluded for all kinetics and crosslinking assays. For cryo-EM data processing, particles that have poor signal to noise ratio, are contaminated or damaged were eliminated using Relion or cryoSPARC.
Replication	Every experiment was repeated at least three times and the outcome from every experiment is included in the result.
Randomization	Randomization is not required since all variables could be controlled.
Blinding	Blinding was not necessary in this study and it was not attempted.

Reporting for specific materials, systems and methods

We require information from authors about some types of materials, experimental systems and methods used in many studies. Here, indicate whether each material, system or method listed is relevant to your study. If you are not sure if a list item applies to your research, read the appropriate section before selecting a response.

Materials & experimental systems		Methods	
n/a	Involved in the study	n/a	Involved in the study
<input type="checkbox"/>	<input checked="" type="checkbox"/> Antibodies	<input checked="" type="checkbox"/>	<input type="checkbox"/> ChIP-seq
<input type="checkbox"/>	<input checked="" type="checkbox"/> Eukaryotic cell lines	<input checked="" type="checkbox"/>	<input type="checkbox"/> Flow cytometry
<input checked="" type="checkbox"/>	<input type="checkbox"/> Palaeontology and archaeology	<input checked="" type="checkbox"/>	<input type="checkbox"/> MRI-based neuroimaging
<input checked="" type="checkbox"/>	<input type="checkbox"/> Animals and other organisms		
<input checked="" type="checkbox"/>	<input type="checkbox"/> Human research participants		
<input checked="" type="checkbox"/>	<input type="checkbox"/> Clinical data		
<input checked="" type="checkbox"/>	<input type="checkbox"/> Dual use research of concern		

Antibodies

Antibodies used	mouse anti-M13 monoclonal antibody (cat: 27-9420-01, GE) a secondary HRP-conjugated Pierce recombinant protein L (cat: 32420, ThermoFisher)
Validation	validations for both antibodies are available on the product website.

Eukaryotic cell lines

Policy information about cell lines	
Cell line source(s)	High Five™ Cells: ThermoFisher, Cat: B85502 Sf9: Expression Systems, Cat: 94-001S.
Authentication	Cell lines were authenticated by the suppliers. No additional authentication was performed.
Mycoplasma contamination	Cell lines are tested by manufacturer for contamination and no additional testing was performed.
Commonly misidentified lines (See ICLAC register)	Name any commonly misidentified cell lines used in the study and provide a rationale for their use.